MODELLING AND EXPERIMENTAL ASSESSMENT OF PUNCHING SHEAR IN FLAT SLABS WITH SHEARHEADS

M.A. Eder[1], R.L. Vollum[1], A.Y. Elghazouli[1], T. Abdel-Fattah[2]

1. Imperial College London

2. Housing and Building Research Centre, Cairo

Abstract

This paper deals with the modelling of punching shear failure in reinforced concrete slabs using non-linear finite element analysis. An analytical procedure is presented for simulating punching failure. The procedure is validated for a large scale reinforced concrete flat slab without shear reinforcement that failed in punching. A parametric analysis is carried out to determine the influence of the key parameters which govern performance. The analytical procedure is then used to model the response of a large-scale hybrid reinforced concrete flat slab specimen tested at Imperial College London which failed in punching. The specimen incorporated a tubular steel column and an ACI 318 type structural steel shearhead. The results of the analysis are used to gain fundamental insights into the contribution of the shearhead to the shear resistance, and to assess the reliability of existing design recommendations for structural steel shearheads.

Key words: Reinforced concrete, slabs, punching shear, structural steel shearheads, non-linear finite element analysis, design codes, Eurocode 2, ACI 318

1. INTRODUCTION

The concrete constitutive models typically used in non-linear finite element analysis (NLFEA) can be broadly categorised as: a) plasticity models, b) damage continuum models and c) coupled plasticity and damage models. Cracking can be modelled with either discrete or smeared crack approaches. Discrete crack approaches are complex since the mesh becomes discontinuous after cracking due to node separation. This requires the fracture process zone of the propagating crack to be adaptively re-meshed in order to capture near crack tip singularities. The difficulties of re-meshing are avoided in the extended finite element method (XFEM), which is based on the concept of partition of unity (Belytschko and Black [1]) and the smeared crack approach of Hillerborg et al. [2] amongst others. The smeared crack approach can be further divided into fixed, rotating, multiple fixed and micro-plane models. Numerous investigators including Abbasi et al. [3], Dyngeland et al [4] Xia and O'Flaherty [5], Hallgren and Bjerke [6] and Zheng et al. [7] have modelled punching shear with varying degrees of success using both solid and shell elements. Available studies in the literature show that numerical modelling of punching shear failure involves complex considerations that require further investigation. It is clear that the constitutive model for concrete should reasonably reflect its tri-axial behaviour since punching is a three-dimensional problem. Furthermore, as expected, solid elements would predict the response more accurately than shell elements. There do not appear to be any significant differences, however, between the performance of plasticity and damage based models. The predicted response appears to be very dependent on the assumed tension softening behaviour which is commonly modelled using the equivalent fracture energy approach. Importantly, the shear retention factor requires careful consideration in fixed crack models. Investigators such as Hallgren and Bjerke

[6] have used rotating crack models to eliminate the shear retention factor and avoid shear stress locking in cracks.

2. NUMERICAL MODELLING

The commercially available finite element program DIANA v9 [8] was used to carry out the numerical analyses described in this paper. The concrete behaviour was modelled with the 'total strain model' (TS-model) in DIANA which is based on the modified compression field theory of Vecchio & Collins [9] and its 3-D extension by Selby & Vecchio [10]. The model is a non-local elastic continuum damage model based on the concept of hypo-elasticity. The stress increments are calculated in terms of strain increments according to $d\sigma_{ij} = C_{ijkl}\, d\varepsilon_{kl}$ where C_{ijkl} is defined as a function of stress, strain, fracture criteria, loading/unloading parameters and others. In this context, $C_{ijkl} \neq C_{klij}$, which means that the stress-strain relationship is load path dependent. Unloading and reloading were modelled with a secant approach.

2.1 Concrete compressive behaviour

The concrete compressive behaviour was described with the following parabolic hardening and softening relationship proposed by Feenstra [11]:

$$\sigma_{(\varepsilon)} = -\frac{f_c \varepsilon}{3\varepsilon_{c/3}} \qquad \varepsilon_{c/3} < \varepsilon \leq 0 \quad (1)$$

$$\sigma_{(\varepsilon)} = -\frac{f_c}{3}\left(1 + 4\left(\frac{\varepsilon - \varepsilon_{c/3}}{\varepsilon_c - \varepsilon_{c/3}}\right) - 2\left(\frac{\varepsilon - \varepsilon_{c/3}}{\varepsilon_c - \varepsilon_{c/3}}\right)^2\right) \qquad \varepsilon_c < \varepsilon \leq \varepsilon_{c/3} \quad (2)$$

$$\sigma_{(\varepsilon)} = -f_c\left(1 - \left(\frac{\varepsilon - \varepsilon_c}{\varepsilon_u - \varepsilon_c}\right)^2\right) \qquad \varepsilon_u < \varepsilon \leq \varepsilon_c \quad (3)$$

$$\sigma_{(\varepsilon)} = 0 \qquad \varepsilon_u < \varepsilon \qquad (4)$$

The three characteristic strains $\varepsilon_{c/3}$, ε_c and ε_u are defined as follows:

$$\varepsilon_{c/3} = -\frac{f_c}{3E} \qquad (5)$$

$$\varepsilon_c = -\frac{5f_c}{3E} \qquad (6)$$

$$\varepsilon_u = \varepsilon_c - \frac{3G_c}{2hf_c} \qquad (7)$$

where $\boldsymbol{\varepsilon}_c$ denotes the peak strain, $\boldsymbol{\varepsilon}_u$ is the ultimate strain, f_c is the concrete compressive strength, E is the elastic modulus, G_c denotes the fracture energy in compression and h is the characteristic length or crack-bandwidth.

The area below the softening part of the compressive stress-strain curve equals G_c/h. The compressive fracture energy G_c is difficult to measure due to its strong dependency on testing procedure but appears to be 100-500 times greater than the tensile fracture energy G_f. Little advice is available in the literature on the choice of G_c. However, the failure loads of the models analysed in this paper are largely insensitive to G_c which was varied between 100 G_f and 200G_f in this work.

The increase in concrete compressive strength with isotropic stress was modelled with the four-parameter Hsieh-Ting-Chen [12] (equation (8)) failure surface which is used in the Selby and Vecchio [10] model to determine the major compressive stress σ_3 required to cause failure. This stress is assumed to be the peak stress of the base curve defined in Equations (1)-(4). The peak strain is also modified depending on the peak stress factor defined in equation (9).

$$f = a\frac{J_2}{f_c^2} + b\frac{\sqrt{J_2}}{f_c} + c\frac{\sigma_1}{f_c} + d\frac{I_1}{f_c} - 1 = 0 \qquad (8)$$

$$K_\sigma = -\frac{f_{3cf}}{f_c} \tag{9}$$

where I_1 denotes the first invariant of the stress tensor, J_2 the second invariant of the deviatoric stress tensor, σ_1 is the maximum principal stress and f_c is the uniaxial compressive strength. The material constants a=2.0108, b=0.9714, c=9.1412 and d=0.2312 were calibrated with data from material tests. The reduction in compressive strength due to lateral cracking was modelled in accordance with the recommendations of Vecchio & Collins [9].

The current work uses a secant implementation of the total strain model in which the concrete is considered as an orthotropic material with $\nu_{ij} = 0$ (Equation 10). The symmetry of the material stiffness matrix retains the symmetry of the global stiffness matrix which is desirable from a computational point of view.

$$D_c' = \begin{bmatrix} E_{c1} & 0 & 0 & 0 & 0 & 0 \\ 0 & E_{c2} & 0 & 0 & 0 & 0 \\ 0 & 0 & E_{c3} & 0 & 0 & 0 \\ 0 & 0 & 0 & G_{c12} & 0 & 0 \\ 0 & 0 & 0 & 0 & G_{c23} & 0 \\ 0 & 0 & 0 & 0 & 0 & G_{c13} \end{bmatrix} \tag{10}$$

where the secant moduli are functions of the stress and strain tensor in the principal coordinate system as follows:

$$E_{ci} = \frac{\sigma_i}{\varepsilon_i} \tag{11}$$

$$G_{cij} = \frac{E_{ci} E_{cj}}{E_{ci} + E_{cj}} \qquad (i \neq j) \tag{12}$$

where ε_i are total strains including non stress-related strains (due to prestressing, thermal expansion, etc.).

The Poisson's ratio of a material determines the lateral displacement of a specimen subjected to uniaxial tensile or compressive loading. A passive lateral confinement acts on the specimen if these displacements are constrained. This effect is important in the three-dimensional modelling of reinforced concrete structures. In the work of Selby and Vecchio [10], this effect is modelled through a pre-strain concept in which the lateral expansion effects are accounted for with an additional external loading on the structure.

2.2 Smeared crack concept

A smeared fixed crack model was used in the current work in which the stress-strain relationships were evaluated in the directions of the principal axes at first cracking (Rankine failure criterion). The crack direction was fixed upon cracking and stresses were calculated in terms of total strains. Up to two further crack planes can form perpendicular to the initial crack plane in 3D analyses. The crack bandwidth defines the length over which the crack width w is smeared at every integration point within the element. This ensures that the cracking process at the integration point always releases the same amount of fracture energy independently of the element size. Theoretically, the crack bandwidth depends not only on the element size but also on its shape, the orientation of the crack within the element and the integration scheme. In this work, the crack band width was taken as the characteristic length $h = \sqrt[3]{V}$ (V= volume of the element) for simplicity.

A constant shear retention factor β was used in the current work to model the reduction in shear stiffness in the post crack regime. The shear moduli (equation 12) are reduced after cracking according to $G^{cr} = \beta G$ with $0 \le \beta \le 1$.

2.3 Concrete Tensile Behaviour

The unconfined uniaxial tensile stress-strain diagram is defined in terms of the concrete tensile strength f_t and its fracture energy in tension G_f. The stress-strain relationship was assumed to be linear in tension until cracking. G_f is a material constant equal to the amount of energy required to create one unit area of crack surface which is defined as follows:

$$G_f = h\int_a^b \sigma_{nn}^{cr}\left(\varepsilon_{nn}^{cr}\right)d\varepsilon_{nn}^{cr} \tag{13}$$

with the limits $a = \varepsilon_{nn}^{cr} = 0$ and $b = \varepsilon_{nn}^{cr} = \infty$

where σ_{nn}^{cr} denotes the post-peak crack stress and ε_{nn}^{cr} denotes the crack strain.

The ultimate tensile strain at which the tensile stress reaches zero $\varepsilon_{nn,ult}^{cr}$ can be computed as follows:

$$\varepsilon_{nn,ult}^{cr} = \frac{G_f}{\alpha h f_t} \tag{14}$$

where G_f depends on the concrete strength and the aggregate size. The following equation from MC90 [13] was used to estimate G_f in this work:

$$G_{f0} = 0.0204 + \frac{0.0053 d_{\max}^{0.95}}{8} \tag{15}$$

$$G_f = G_{f0}\left(\frac{f_{cm}}{f_{cm0}}\right)^{0.7} \tag{16}$$

where d_{max} is the maximum aggregate size, f_{cm} is the mean concrete compressive strength and f_{cm0}=10 MPa. The coefficient α in equation (14) is defined as follows:

$$\alpha = \int_{x=0}^{x=\infty} y(x)dx \qquad (17)$$

where *y(x)* is the assumed tension softening function.

3. PUNCHING SHEAR BEHAVIOUR OF RC-FLAT SLAB SUB ASSEMBLAGE

The numerical model was validated for a slab without shear reinforcement tested in punching by Vollum et al [14]. The slab (see Fig. 1) measured 3m square by 220mm thick and was centrally loaded from the bottom through a 270mm square steel plate. The slab was vertically restrained by 16 ties positioned around its perimeter as shown in Fig. 1. The tensile reinforcement consisted of T16 bars at 90mm centres in each orthogonal direction. The compression reinforcement consisted of T10 bars at 180mm centres in each orthogonal direction. The mean concrete cube strength was f_{cu}=30MPa. The concrete cylinder strength was taken as $0.8f_{cu}$ = 24 MPa in accordance with MC90 [13]. The maximum aggregate size was 20mm. The cover to the top and bottom reinforcement was 35mm.

One quarter of the specimen was modelled with the gradated mesh shown in Fig. 2 which is refined around the loading platen. Seven elements were used through the depth of the slab. The reinforcement was modelled with discrete truss elements assuming perfect bond. The horizontal displacements were restrained in the X and Y directions perpendicular to the axes of symmetry. The slab was vertically restrained around its perimeter at the positions of the tie down bars. The concrete and loading plates were modelled with 20-noded isoparametric brick elements. The reinforcement

was modelled with 3-noded 3D cable elements and the struts were modelled with 2-noded 3D truss elements. The concrete was modelled with the TS-fixed crack model, the plates and struts were assumed to be linearly elastic and the reinforcement was modelled as elasto-plastic with the Von-Mises yield criterion. The total number of elements was 10459 and the total number of nodes was 39942. A full 3x3x3 integration scheme was adopted for the solid elements within the zone where the mesh was refined around the column. A 2x2x2 reduced integration scheme was used elsewhere.

3.1 Methodology

A quasi-Newton (secant) iteration solution procedure was used with an iterative based step size solver. The slabs were loaded in two-phases to simulate the test procedure. The slab self-weight was activated in the first phase of the analysis in which the slab was supported on the central loading platen. The elements representing the steel bearing plates at the edge of the slab were activated in the second phase of the analysis along with the corresponding vertical restraints. Load control was used in the first phase and displacement control subsequently. The vertical displacement was assumed to be zero at the centre of the bearing plates whereas in reality the rig was designed to ensure that the vertical reactions were equally distributed between the 16 restraining tie bars placed around the perimeter of the slab. An energy based convergence criterion was used with a tolerance value of 1×10^{-3}.

3.2 Baseline analysis

A baseline analysis was carried out with the concrete material parameters listed in Table 1 which are discussed in the sensitivity studies presented below. Fig. 3

compares the measured and predicted load displacement responses for slab S1. The slab was predicted to fail at a load of 642 kN compared with the measured failure load of 614 kN. The deviation between the measured and predicted capacity is 4.4% with a 6.5% deviation in displacements.

3.3 Sensitivity studies

A series of sensitivity studies were undertaken in which one parameter was varied at a time with all the other parameters held constant at the values given in Table 1. The sensitivity study examined the effect of varying all the input parameters but results are only presented for the concrete tensile strength, tension softening relationship, shear retention factor and mesh density which were found to be most significant. It is useful to discuss the results of the sensitivity study with reference to the idealised load displacement diagram shown in Fig. 4 which is divided into four zones. The response is linear elastic in Zone 1 prior to cracking. In Zone 2, radial cracks initially form around the column, followed by circumferential cracks, both of which cause a distinct softening of the structure. The response is almost linear in Zone 3 which is characterised by the propagation of existing cracks through the depth of the slab with only a few new cracks being initiated. The load-displacement graph flattens at failure which occurs in Zone 4 and is characterised by unstable crack propagation under constant load. The tensile reinforcement typically de-bonds in Zone 4 as the tensile cracks propagate along the interface between the reinforcement and the concrete below eventually leading to total failure.

3.3.1 *Concrete tensile strength*

The concrete tensile strength was varied between 1.0 and 3.0 MPa whilst maintaining the other material parameters at the values used in the base study. The results are presented in Fig. 5 which shows that increasing the concrete tensile strength from 1.0 to 3.0 MPa affected the displacements much more significantly than the failure load. Fig. 5 shows that increasing the concrete tensile strength delayed the crack initiation and reduced displacements by shifting the load displacement curve to the left whilst maintaining the slope of load displacement curve in Zone 3. The concrete tensile strength of 1.5MPa used in the baseline analysis is around 60% of the splitting strength calculated with MC90 [13] but similar to that given by the following equation from ACI 209 Model Code [15]:

$$f_t = 0.0069\sqrt{w\ f_c} \quad \text{[MPa]} \qquad (18)$$

where w is the concrete density in kg/m^{3}and f_c is the concrete cylinder strength.

The concrete tensile strength of 1.5 MPa used in the baseline analysis corresponds to $f_t = 0.30\sqrt{f_c}$ and is similar to the tensile strength of $f_{ct}=0.33f_c^{1/2}$ recommended by Bresler & Scordelis [16] for the NLFEA of shear failure in beams and subsequently used by Vecchio and Shim [17] amongst others. The tensile strengths used in the analysis are also comparable with the results obtained by Lee et al. [18] in a series of direct tension tests on large-scale normal-weight concrete specimens (specimen size = 1400mm long × 1100mm wide x 250mm thick) in which they found that the direct tensile strength was about half the indirect tensile strength of cylindrical specimens. The direct tensile strengths f_t [Mpa] measured in Lee et al.'s [16] tests ranged from $f_t = 0.27\sqrt{f_c}$ to $f_t = 0.37\sqrt{f_c}$ with a mean of $f_t = 0.30\sqrt{f_c}$ which is comparable with the strengths given by equation (18). The authors' suggest that the

concrete tensile strength should be taken between 45-60% of the indirect concrete tensile strength in NLFEA of punching shear.

3.3.2 Concrete tension softening response

The effect of varying the softening response was investigated by carrying out analyses on slab S1 with brittle (G_f=0), perfectly-plastic (G_f= ∞), linear, exponential and Hordijk [19] tension softening functions. The other material parameters had the values used in the base study. The brittle and constant softening responses were chosen to represent extreme lower and upper limits. The ultimate crack strain was chosen to make the area under the tensile stress crack strain curve equal to G_f/h in the linear, exponential and Hordijk [19] models. The exponential softening function can be expressed as follows:

$$f_t(\varepsilon) = f_t e^{-\frac{\varepsilon}{\kappa}} \tag{19}$$

$$\kappa = \frac{G_f}{h f_t} \tag{20}$$

where ε denotes the tensile crack strain. The exponential softening function was found to be more stable numerically than the linear or Hordijk [19] tension softening responses since the strength asymptotically approaches zero. The brittle tension softening model was the least stable.

Fig. 6 shows that the assumed tension softening behaviour has a significant effect on the overall performance. Flexural failure occurred when the concrete tensile stress was maintained at the concrete tensile strength after cracking. The shear strength of the tested slab was significantly underestimated when the concrete was assumed to be brittle in tension with the stress dropping immediately to zero after

cracking and there was no sign of the softening Zone 2 in the load-displacement response. Fig. 6 shows that the area under the tension softening diagram should be related to G_f/h as in the linear, exponential and Hordijk [19] models. Significantly, the shape of the softening diagram had no significant influence on the predicted performance in the present study.

3.3.3 Shear retention factor β

The literature gives no definitive guidance on the best choice of β since its affect varies with structural form, reinforcement arrangement and the chosen concrete constitutive model. For example, the shear retention factor has no influence on the failure load or deformation of a single isotropically reinforced quadrilateral element loaded in pure shear since the shear stress parallel to the crack is zero. Such an element fails in tension when the maximum principal stress exceeds its tensile strength ($\tau_{max} = \sigma_1 = f_t$) with the post-failure response being governed by the assumed tension softening response. An isotropic element is only influenced by β when loaded in pure shear if the element is pre-cracked with the cracks skew to the principal compressive stress field for pure shear. In this case, the slope of the load displacement diagram is proportional to β. A series of axi-symmetric analyses were made to investigate the effect of varying β on punching shear capacity. The results showed that increasing β increases the failure load by delaying the fracture process and, thereby, alleviating the shear stresses in the uncracked concrete. Increasing β had progressively less effect on the failure capacity as the flexural reinforcement ratio was reduced and no effect in plain concrete punching specimens.

The study was then extended to investigate the effect of varying β from 0.01 to 1.0 on the response of Slab S1. The other material parameters were unchanged

from the values used in the base study (see Table 1). The results are shown in Fig. 7 which shows that the failure load increased by almost 100% as β was increased from 0.01 to 1.0. Furthermore, increasing β had relatively little effect on the slope of the load deflection response within Zone 3 (see Fig. 4 for definition) but increased the length of Zone 3.

The best choice of β seems to depend on many factors including the type of structure and its failure mode in addition to the concrete properties and software formulation. Rots [18] recommends that relatively low shear retention factors should be used in fixed crack models to avoid stress locking. The optimum value of β is problem dependent as discussed above and needs to be investigated on a case by case basis. The best choice of β was found to be in the range $0.1 \le \beta \le 0.25$ in the current work, which is within the range reported by other researchers [18].

3.3.4 Mesh density

In the "original" mesh (see Fig. 2), seven layers of elements were used through the depth of the slab. The smallest elements measured 22.5x22.5mm on plan x12mm thick and the largest measured 90x90x43mm. Seven layers of elements were also used in the "coarse mesh" in which the dimensions of the elements around the column were increased from 22.5x22.5mm to 45x45mm on plan. No other changes were made to the mesh which included 10045 nodes and 3064 elements. The "fine depth" mesh had the same element dimensions on plan as the "original" mesh but the number of layers of elements was increased from three to five between the reinforcement layers giving a total of nine layers of elements with 50174 nodes and 12909 elements.

Fig. 8 shows that the performance of the model was objective in the sense that the numerical results converged as the mesh was refined and that decreasing the mesh

density increased the failure capacity. The coarse mesh gave an overly stiff response in both the pre-and post-damage regimes due to discretisation errors which led, initially, to delays in crack initiation and, subsequently, to variations in crack strain concentrations from denser meshes. The computational efficiency was found to reduce significantly, in the present study, when the number of nodes was increased above around 40000. Therefore, the baseline mesh was adopted for the parametric studies since it gave very similar results to the fine mesh (see Fig. 8) but significantly shorter runtimes.

4. EXPERIMENTAL RESPONSE OF HYBRID FLAT SLAB SYSTEM

A large scale hybrid flat slab was tested in the structural laboratories at Imperial College London as part of an investigation into punching shear failure. The specimen (H1) was attached to a steel column with an ACI 318 [21] type structural steel shearhead made from pairs of 51x38 rolled steel channels welded back to back. The specimen measured 3270mm × 2900mm on plan with a slab depth of 155mm. Details of the specimen and flexural reinforcement are given in Figs. 9 and 10 respectively. T12 bars at 100mm centres were used in each orthogonal direction for the tension reinforcement and T12 bars at 200mm centres for the compression reinforcement.

The mean concrete cube and split cylinder tensile strengths were f_{cu}= 47.4 MPa and $f_{t\text{-}split}$=3.3 MPa respectively. The concrete cylinder strength was taken as $0.8f_{cu}$ = 38 MPa in the analysis. The average yield strength of the steel in the 51×38 RSC was measured in coupon tests to be 300 MPa. Stress strain curves for RSC and the 12mm diameter flexural reinforcement bars are given in Figs. 9c and 9d respectively. The strains were measured with a video extensometer in the material tests and with surface mounted electrical resistance strain gauges in the tested slab.

The cover was 20mm to the top and bottom reinforcement. The column consisted of a 180x180x10 square hollow section. The connection between the shearhead and column was strengthened with 8 mm thick polygonal shaped gusset plates which were fillet welded to the top and bottom flanges of the channel sections. The gusset plates were designed to prevent local buckling of the column by smoothly transferring forces from the flanges of the shearhead into the column. The shearhead was centrally embedded in the slab between the four layers of reinforcement. The slab edges (see Fig. 9) were supported with 4 pin ended members, which were connected to bearing beams made from pairs of PFC-180 channels that distributed the reaction forces along the slab edges.

4.1 Test results

The load was applied from the bottom in 100 kN steps. At each load step, cracks were marked, crack widths were measured at three locations above the shear arms and surface strains were measured with a DEMEC gauge. Radial cracks, which propagated from the column, were first observed at a load of 100kN. Tangential cracks were first observed at a load of 200kN. A regular crack pattern developed as the load increased and the slab failed in punching at a load of 453kN (see Fig. 11). The failure perimeter was much larger than predicted by ACI 318 [21] when viewed from above. It seems likely that a smaller and steeper punching cone developed inside the slab within the externally visible failure perimeter and that the shear crack changed direction when it reached the tensile reinforcement. The compressive surface was completely intact at failure. The yellow dotted line in Fig. 11 represents the assumed extension of the visible failure perimeter, based on acoustic examination. Fig 12 shows the shearhead at the end of the test after it was extracted from the specimen.

The permanent deformation suggests that the shearhead arms deformed plastically before punching failure occurred.

4.2 Numerical model

One quarter of the specimen was modelled with the finite element mesh shown in Fig. 13 which included 10509 elements and 39411 nodes. The mesh was refined in plan around the column and included 8 layers of elements through the slab depth. The influence of mesh refinement was investigated for slab H1 amongst others. The analyses showed that the mesh should be refined around the shear arms as shown in Fig. 13a with the zone of mesh refinement extending beyond the tips of the shear arms, by around twice the slab depth, if shear failure occurs outside the shearhead. Full (3×3×3) integration should be used within the refined zone of the mesh to avoid convergence problems. The model cannot capture punching shear failure if the mesh is too coarse in which case flexural failure is almost always predicted.

The steel sections were modelled with 6 noded triangular and 8 noded quadrilateral Mindlin-Reissner isoparametric shell elements. A 3x3x3 integration scheme was used in the refined zone of the mesh around the column and in the shell elements. A 2x2x2 integration scheme was used elsewhere. Horizontal displacements were restrained in the X and Y directions perpendicular to the axes of symmetry with the shell elements restrained with additional rotational restraints. The slab was restrained vertically around its perimeter at the tie locations shown in Fig. 9a. Finally the centre point of the bottom column plate was restrained in the X, Y and Z directions. Perfect bond was assumed between the shearhead and the concrete. The Von-Mises yield criterion with linear isotropic hardening was adopted for the shearhead. Results are presented for: a) a baseline analysis in which β and f_{ct} were chosen to give a good fit with the measured

load-displacement response and b) a “sensitivity” analysis in which the material parameters were either the same or had the same relationship with the concrete cylinder strength as in the baseline analysis of Slab S1. Table 2 shows the concrete material properties and shear retention factors used in the “sensitivity” and “best fit” analyses for slab H1. The use of the same concrete tensile strength in the “best fit” analyses for slabs S1 and H1 is coincidental and at first sight unexpected since slabs S1 and H1 had concrete cylinder compressive strengths of 24 and 38 MPa respectively. It should however be noted that the tensile strength of 1.5 MPa used in the “best fit” analyses is relatively close to the value of 1.89 MPa calculated for the “sensitivity” analysis of slab H1 (see Table 2) in terms of the concrete compressive strength. Furthermore, deflections depend on test specific factors such as the loading rate and the effective insitu concrete tensile strength, which is affected by curing and reduced by tensile stresses induced by restrained shrinkage. The concrete elastic moduli of 13.5 GPa and 21.1 GPa used in the analyses of slabs S1 and H1 respectively were calculated with equation (6) assuming that the concrete reached its uniaxial cylinder strength at a strain ε_c= -0.003. Parametric studies were carried out to investigate the effect of varying ε_c between -0.002 and -0.003 where ε_c is the uniaxial strain at the peak stress f_c. The failure load was found to be virtually insensitive to ε_c which was taken as -0.003 for slabs S1 and H1 since this gave the best estimates of slab deflection. The concrete elastic moduli used in the analyses of slabs S1 and H1 respectively are a consequence of taking ε_c as -0.003 in equation (6). The concrete elastic modulus is estimated to have been around 25 GPa for slab S1 which is rather higher than used in the NLFEA. Three companion control cylinders were tested to determine the elastic modulus for slab H1. The resulting mean concrete stress-strain curve was linear up to a stress of around $0.4f_c$ with an elastic modulus of 29 GPa. The

concrete reached its peak stress at a strain of ε_c= -0.0023. The secant moduli used in the NLFEA of slab H1 were ~73% of the measured values for stresses up to f_c, primarily due to the choice of ε_c= -0.003 in equation (6). The good correspondence between the measured and predicted deflections for slabs S1 and H1 suggests that the elastic moduli used in the analyses are reasonable for the tested slabs. The reduced effective concrete elastic modulus in the slabs is largely attributable to the effect of creep and loss of tension stiffening under sustained load whilst cracks were marked after each loading increment. The reduction in stiffness would have been proportionally greatest for slab S1 due to its low concrete strength.

4.3 Comparative Results

Fig. 14 shows that the baseline load-displacement response agrees well with the measured response. The shear strength was overestimated in the "sensitivity" analysis primarily due to the increase in β from 0.1 to 0.25. This shows that the "best fit" input parameters for the finite element analysis vary with changes in model geometry largely since β is a structural rather than material parameter. For a given concrete compressive strength, default values can be used for all the parameters in Tables 1 and 2 except the concrete tensile strength and the shear retention factor β which have the most significant effect on the load-displacement response. A "best fit" can be obtained with test data by choosing a) the concrete tensile strength to match the load-deflection response within Zone 2 of Fig. 4 and b) the shear retention factor to match the measured failure load. The authors [14] have shown elsewhere that once validated for a particular test setup the numerical procedure can, for given β and f_{ct}, reliably predict the effect of changing the area of flexural reinforcement and adding shear reinforcement. The failure load of 432 kN computed in the baseline analysis is 5%

less than the measured failure load of 453 kN. The computed displacement is 6% less than measured at failure. First yielding of the tensile reinforcement was predicted to occur adjacent to the column at 408 kN. This is consistent with the test where the reinforcement only yielded locally around the column in the test and no distinct yielding zone was observed.

Fig. 15 shows that significant plastic strains were predicted to develop in the tensile flange and web of the shearhead at failure but not in the compression flange indicating composite action with the slab. Fig 16 shows the measured and computed axial strains ε_{xx} in the top and bottom flanges of two mutual perpendicular shear arms. The positions of the strain gauges are shown in Fig. 9b. The measured and computed strains agree reasonably well in the compressive regime (positive) until near failure but the tensile strains diverge at a load of approximately 250kN. The divergence is thought to be due to bond slip between the tensile flange and the surrounding concrete which the continuous mesh formulation could not capture. Fig. 16 also shows that both the tensile and compressive flanges yielded at failure in the test.

Fig. 17 shows the axial strain distribution ε_{xx} in the concrete through the depth of the slab at 4 points (see Fig. 9a) adjacent to the intersection between the shear arm and the outer face of the gusset plate at the ultimate load. The vertical lines show the positions of the flexural reinforcement and the centrelines of the flanges of the shearhead. The presence of shear strains caused the axial strain distribution to deviate from the Kirchhoff hypothesis. The tensile flange of the shearhead appears to have locally controlled crack widths in the concrete since the strain at the level of the tension reinforcement increases from $\boldsymbol{\varepsilon}_{xx}$= 0.0014 within the width of the tensile flange to $\boldsymbol{\varepsilon}_{xx}$= 0.0053 outside the section. The kink in the tensile strain distribution at the level of the reinforcement is attributed to the failure of the smeared crack

approach to model the slip between the tensile flange of the shearhead and the surrounding concrete. Fig. 17 also shows that a compression zone of fairly uniform depth formed in the concrete below the compression flange of the shearhead and that the compressive strain reduced to near zero in the concrete below the compression reinforcement.

Fig. 18 shows contour levels at the ultimate load for horizontally aligned Mode-1 tensile cracks in the concrete layer surrounding the bottom reinforcement. The cracking is consistent with that observed in the test at failure where the column and upper part of the slab became detached from the compressive surface below which was left intact. The analysis suggests that the cracking initiated at the gusset plates which formed a horizontal discontinuity in the slab. The horizontal cracking in the reinforcement layer appears to explain the drop in the compressive strain below the flange indicated in Fig. 17. The influence of the gusset plates on the distribution of ε_{xx} through the slab depth at the column face was investigated by re-analysing Slab S1 with a structural steel shearhead that measured 1080 mm from tip to tip. The cross-section of the shearhead was an "I" section with an overall depth of 97mm and 180mm wide. The flange was 8mm thick and the web was 12 mm thick. The shearhead increased the computed failure load of S1 from 642kN to 800kN. Figs. 19a and 19b respectively show the resulting strain distributions at 3 points adjacent to the column face (see Fig. 1) for the baseline model without and with the shearhead. Comparison of the two figures shows that the maximum compressive strain occurred at the extreme compressive fibre and that the presence of the shearhead evened out the strain distribution across the width of the column. Comparison of Figs. 17 and 19b supports the hypothesis that the gusset plates caused the compressive strain to reduce to near zero in the concrete below the compressive flange of the shearhead.

4.4 Factors influencing the load distribution on the shearhead

This section examines the shape of the loading distribution along the arms of the shearhead and the influence of the length and relative stiffness of the shearhead arms. The shear force was calculated at intervals along the arms of the shearhead by numerically integrating the computed shear stresses. Fig. 20 shows that the arms collected vertical loads gradually since the shear force is not uniformly distributed along the arms as would be the case if the load was applied at the ends of the arms. The bending moment was calculated at intervals along the shearhead arms by a) numerically integrating the axial stresses computed in the finite element analysis and b) by integrating the shear force distributions shown in Fig. 20. Fig. 21 shows that the arms of the shearhead acted compositely with the slab since the bending moments calculated with procedure a) above are less than those calculated with procedure b). This conclusion is consistent with the observation that a significant tensile force of 126 kN was computed to develop at failure in each arm at the intersection with the face of the gusset plate. Fig. 21 also shows that the bending moments computed with procedure a) can be conservatively estimated with a triangularly distributed load that decreases from a maximum at the tip of the shear arms to zero at the intersection with the gusset plates. The bending moments from procedure b) above are considered appropriate for design since the degree of composite action is uncertain in reality. The total shear force resisted by the four arms of the shearhead was ~124 kN (or 27% of the failure load) at the outer edge of the gusset plates. This implies that the greater part of the load was transferred into the column through the concrete at the perimeter of the gusset plate.

4.5 Modelling of slabs tested by others

The NLFEA procedure was further validated by modelling 3 slabs with concrete columns and structural steel shearheads tested by Corley and Hawkins [22]. Specimens BN1, BH2 and BH3 were analysed. Full details of the specimens are given elsewhere [22]. Specimen BN1 was a control specimen without a shearhead. Specimens BH2 and BH3 were reinforced with shearheads with the configuration shown in Fig. 22a. The same "I" section was used for the arms of the shearhead in each specimen but the length of the shearhead was doubled in test BH3. All three specimens failed in punching shear. Table 2 gives the material properties used in the analysis. Table 3 shows that the analyses accurately predicted the measured failure loads. Fig. 20b shows the predicted variation in shear force along the shearhead arms in tests BH2 and BH3. The analyses suggest that the shear force was introduced primarily into the tips of the shearhead in BH2 but more uniformly along the length of the arms in specimen BH3 in which the shearhead was twice as long. In both cases, shear forces were transferred back into the slab from the shearhead near the column. Bending moments were calculated at the column face by integrating the axial stresses in the shearhead. Table 3 shows that the resulting bending moments compared well with those derived by Corley and Hawkins [22] at the ultimate load from the measured strains.

5. REVIEW OF DESIGN RECOMMENDATIONS FOR SHEARHEADS

The tests of Corley et al. [22] and Chana and Birjandi [23] show that shearheads increase punching capacity by enlarging the critical shear perimeter in much the same way as a larger column. Corley et al. [22] defined shearheads as over-reinforcing if the flexural capacity of the shearhead was not reached before the end of the test and

under-reinforcing if the flexural capacity was reached before the end of the test. The test data [22], [23] suggests that the failure surface follows the perimeter of the shearhead for over-reinforcing shearheads but falls inside the ends of the shearhead for under-reinforcing shearheads. The punching shear strength of a slab reinforced with a shearhead can be expressed as:

$$V_u = KV_{Rdc} + V_{sh} = V_{out} \quad (21)$$

where K is an efficiency factor, V_{Rdc} is the shear resistance provided by the concrete without the shearhead, V_{sh} is the contribution of the shearhead and V_{out} is the shear resistance of the enlarged failure surface. The basic shear resistance without the shearhead V_{Rdc} is calculated as follows in EC2 [24]:

$$V_{Rdc} = v_{Rdc} U_1 d \quad (22)$$

where v_{Rdc} is the shear resistance provided by the concrete, d is the effective depth and U_1 is the basic shear perimeter which is calculated as follows:

$$U_1 = U_{col} + 4\pi d \quad (23)$$

where U_{col} is the perimeter of the column.

$$V_{out} = v_{Rdc} U_{out} d \quad (24)$$

where U_{out} is the perimeter of the enlarged failure surface.

5.1 ACI 318 [21] design method

ACI 318 [21] gives a design method for shearheads which is based on the work of Corley et al. [18] in which the punching shear resistance is calculated as follows:

$$V_u = \frac{\sqrt{f_{ck}}}{3} U_{out} d \quad (25)$$

where U_{out} is the critical shear perimeter defined in Fig. 22a. The plastic moment of resistance of the shear head arms is calculated with Equation 11-37 in ACI 318 [21]

which is derived from the idealised shear force distribution shown in Fig. 22b with $V_{Rdc} = 0.5V_u$ .The coefficient α_v in Fig. 22a is the ratio between the flexural rigidity of each shearhead arm and that of the surrounding composite cracked slab (including the shearhead) of width $h_{col}+d$ where h_{col} is the column width perpendicular to the shearhead. The enlarged shear perimeter U_{out} is assumed to be critical provided the plastic moment of resistance of the shearhead arms satisfies equation 11-37 in ACI 318 and $\alpha_v \geq 0.15$.

5.2 Chana and Birjandi [23] design method

Chana and Birjandi [23] developed an alternative design method for structural steel shearheads on the basis of 19 tests they carried out on large as well as small scale specimens. The method is applicable to both ACI 318 type shearheads (see Fig. 22c) and shearheads enclosed with secondary arms (see Fig. 22d). For shearheads without openings adjacent to the column, the method is equivalent to assuming $K=1$ and $V_{sh} = nM_p/L$ in Equation (21) where M_p is the plastic moment of resistance of each shearhead arm, n is the number of arms and L is the extension of the arms from the column face. The critical outer shear perimeter U_{out} is calculated as shown in Figs. 22c and 22d respectively for ACI 318 type and enclosed shearheads. Chana and Birjandi [21] assumed that shearheads designed for $M_p=LV_{sh}/n$ are sufficiently stiff to push the critical punching shear perimeter outside the shearhead.

5.3 Assessment of design methods with data from Corley and Hawkins [22]

Fig. 23 compares the predictions of ACI 318 and the Chana and Birjandi [23] method with data from 21 slabs tested by Corley and Hawkins [22]. The basic shear strength V_{Rdc} was calculated with EC2 (with γ_c=1.0) in the Chana and Birjandi [23] method

rather than BS8110 [25] as originally used and the effective length of the shearhead arms was taken as the smaller of the actual length or $L^* = 0.5h_{col} + 4M_p/(V_{out}-V_{Rdc})$ in the calculation of U_{out}. The shear force V_{sh} was assumed to be introduced into the shearhead at the effective ends of its arms (i.e. at a distance $L^*-0.5h_{col}$ from the column face). Fig. 23 shows that the Chana and Birjandi [23] method predicts the shear strength more accurately than ACI 318 [21]. Fig. 24 shows that the increase in shear strength provided by the shearhead was significantly greater than $\alpha_v V_{ctest}$ for most of the specimens tested by Corley and Hawkins [22].

5.3.1 *Assessment of tested Specimen H1 with ACI 318*

The tested specimen H1 does not strictly comply with the requirements of ACI 318 since the ratio α_v between the flexural stiffness of each shearhead arm and the surrounding composite cracked slab is ~0.11 which is less than the critical value of 0.15 given in ACI 318. Despite this, the punching shear resistance was calculated with ACI 318 using the full effective depth of d = 123mm and α_v=0.11. The calculated failure load was 650kN which is significantly greater than the measured failure load of 453kN.

5.3.2 *Assessment of tested Specimen H1 with method of Chana and Birjandi [23]*

V_{Rdc} is uncertain for specimen H1 due to the presence of the gusset plate which is analogous to an enclosed shearhead. Therefore, V_{Rdc} was calculated for specimen H1 with a) EC2 for a 180mm square column, b) following Chana and Birjandi's [23] recommendations for an enclosed shearhead with dimensions equal to the gusset plate (see Fig. 22c) with v_{Rdc} from EC2, and c) following the ACI 318 recommendations for a small shearhead with dimensions equal to the gusset plate (for which the punching

capacity of Specimen H1 reduces to that of a 180mm square column). The full effective depth of 123mm was used throughout. The use of ACI 318 to estimate the shear strength without the shearhead is somewhat speculative since ACI 318 does not include provisions for dealing with gusset plates. Precedence for this approach is provided by Corley and Hawkins' [22] analysis of lift slab collars which are analogous to the gusset plates. The basic shear strength v_{Rdc} was calculated with EC2 to be 1.2MPa (with γ_c=1.0). The resulting shear strengths V_{Rdc} of a) 337 kN, b) 320 kN and c) 319 kN are similar to V_{NLFEA}-$V_{shearhead\ NLFEA}$ = 432-124=308 kN. V_{Rdc} was also estimated with NLFEA assuming the shearhead arms stopped at the edge of the gusset plate and was found to be 255kN which suggests that the shearhead increased the computed shear capacity of the surrounding concrete in addition to transferring load directly into the column.

The shear resistance of Specimen H1 was calculated with the Chana and Birjandi [23] method to be 498 kN with V_{Rdc} equal to 320 kN from b) above and 472 kN with V_{Rdc} = 255kN from the NLFEA. The effective length of the shearhead arms was taken as $L_{eff}^* = 0.5h_{col}+4M_p/(V_{out}-V_{Rdc})$ where $V_{out} = v_{Rdc}U_{out}d$. U_{out} was calculated in accordance with Fig. 22c. These estimates compare reasonably well with the measured failure load of 453 kN and are relatively insensitive to V_{Rdc} even though the ratio between the depths of the shearhead and slab is relatively low compared with those in previous tests [22], [23].

5.3.3 Comparison of calculated internal actions in shearhead arms

Figs 20 and 21 compare the shear force and bending moment distributions in the shearhead arms given by NLFEA, ACI 318 and Chana and Birjandi [23] at the failure

load of 432 kN computed in the NLFEA. The ACI 318 bending moments were calculated with both Equation 11-37 in ACI 318 and the shear force distribution shown in Fig. 22b with V_{Rdc}= 255 kN from the NLFEA without the shearhead arms. The effective length of the shearhead arms was taken as $L^* = 0.5h_{col} + 4M_p/(V_{pred} - V_{Rdc})$ in the Chana and Birjandi [23] method with V_{pred}=*432 kN* and V_{Rdc} = *255 kN*. Figs. 20, 21, and 23 suggest that the design method of Chana and Birjandi [23] is more realistic than ACI 318 particularly for relatively light shearheads such as that described in this paper where α_v is less than the limiting value of 0.15 in ACI 318.

6. CONCLUSION

This paper presents a non-linear finite element procedure for simulating punching shear failure in reinforced concrete slabs with and without shearheads. The procedure is shown to accurately predict the measured response of a recent large scale punching test on a slab without shear reinforcement. Sensitivity analyses are presented to show the influence of the concrete tensile strength, shear retention factor and mesh density on the predicted failure load. Tension softening was found to have an even greater affect on the predicted load displacement response than the concrete tensile strength. Good results were obtained when the concrete tensile strength was taken between 0.45-0.6 times the indirect tensile strength. It is shown that the area under the tension softening diagram should be related to the tensile fracture energy G_f and the crack band width but the shape of the softening diagram (i.e. linear, exponential, Hordijk [19]) was not found to have a significant influence on the predicted performance.

Subsequently, the proposed finite element procedure is used to analyse the influence of structural steel shearheads on punching failure. Detailed results are

presented for the analysis of a large scale specimen incorporating a structural steel shearhead tested as part of this investigation. Results are also presented for 3 slabs tested by Corley and Hawkins [22] of which two were reinforced with shearheads. The finite element procedure is shown to give good predictions of the measured shear strengths of all these specimens. The results of the finite element analysis were used to investigate the contribution of the shearhead to the punching shear resistance. The analyses suggest that loads are principally transferred into shearhead at the tips of the arms if the failure surface lies outside the shearhead as shown in Fig. 22c. Load is transferred more uniformly into the arms of the shearhead if the punching failure surface lies within the ends of the shear arms as in the authors' test H1 and test BH3 of Corley and Hawkins [22].

The design methods of ACI 318 [21] and Chana and Birjandi [23] for shearheads are evaluated in the light of the conclusions from the finite element analysis and test data from this programme and Corley and Hawkins . Chana and Birjandi's [21] design method was found to give the best predictions of shear strength.

7. ACKNOWLEDGEMENT

The financial support of Corus and Cidect for the tests described in this paper is gratefully acknowledged. Additionally, the authors would like to thank the technical staff of the Structures Laboratories at Imperial College London, particularly Mr R. Millward, for their assistance with the experimental work. The first author would also like to acknowledge the fees grant awarded to him by EPSRC.

8. REFERENCES

1. Belytschko, T. and Black, T., Elastic crack growth in finite elements with minimal remeshing, International Journal for Numerical Methods in Engineering 45 (5): pp. 601-620, 1999
2. Hillerborg, A., Modeer M., Petersson P-E., Analysis of Crack Formation and Crack Growth in Concrete by Means of Fracture Mechanics and Finite Elements, Cement and Concrete Research, Vol6, pp.773-782, 1976
3. Abbasi, M. S. A., Baluch, M. H., Azad, A. K., Rahman, H. H. A., Nonlinear Finite Element Modelling of Failure Modes in RC Slabs, Computers & Structures, Vol42, No5, pp. 815-823, 1992.
4. Dyngeland, T., Hoiseth, K. V., Opheim, E., Punching Shear of Reinforced Concrete Plates, G.M.A. Kusters and M.A.N. Hendriks (eds.) DIANA Computational Mechanics, pp. 329-338, 1994.
5. Xiao, R. Y., O'Flaherty, T., Finite-element analysis of tested concrete connections, Computers and Structures, Vol78, pp.247-255, 2000.
6. Hallgren, M., Bjerke, M., Non-linear finite element analyses of punching shear failure of column footings, Cement & Concrete Composites, Vol24, pp. 491-496, 2002.
7. Zheng, Y., Robinson, D., Taylor S., Cleland, D., Finite element investigation of the structural behaviour of deck slabs in composite bridges, Engineering Structures, Vol 31, pp. 1762-1776, 2000.
8. DIANA, User's manual Material Library, Release 9.3, May 2008
9. Vecchio, F., and Collins, M. P., The Modified Compression-Field Theory for Reinforced Concrete Elements Subjected to Shear, ACI Journal, Vol. 83, No. 2, pp. 219-231, 1986

10. Selby, R. G., and Vecchio F. J., A constitutive model for analysis of reinforced concrete solids, Tech. Rep. University of Toronto, Can. J. Civ. Eng. 24: 460-470, 1997.
11. Feenstra, P. H., Computational Aspects of Biaxial Stress in Plain and Reinforced Concrete., PhD thesis, Delft University of Technology, 1993.
12. Chen, W. F., Plasticity in Reinforced Concrete, McGraw-Hill Co., New York, 1982, 474 pp.
13. CEB-FIP., CEB-FIP Model Code 1990, Comité Euro-International du Béton, 1993.
14. Vollum, R.L, Abdel-Fattah T., Eder M. and Elghazouli A., Design of ACI type punching shear reinforcement to Eurocode 2, Magazine of Concrete Research, Vol. 62, Issue 1, 3-16, 2009..
15. ACI, Prediction of Creep, Shrinkage, and Temperature Effects in Concrete Structures, Tech. Rep. ACI 209R-82, American Concrete Institute, 1982.
16. Bresler B. and Scordelis A.C., Shear strength of reinforced concrete beams. Journal of Americal Concrete Institute, 60(1), 1963: pp. 51-72.
17. Vecchio F.J., Shim W., "Experimental and analytical re-examination of classic concrete beam tests", Journal of Structural Engineering, Vol. 130, No. 3, March 2004, pp. 460-469.
18. Lee S.-K, Woo S.-K and Song Y.-C Softening response properties of plain concrete by large-scale direct tension tests, Magazine of Concrete Research, Vol. 60, No. 1, 33-40, 2008.
19. Cornelissen, H. A. W., Hordijk, D. A., AND Reinhardt, H. W., Experimental determination of crack softening characteristics of normal weight and lightweight *concrete*, Heron, Vol. 31, No. 2, 1986.

20. Rots, J. G., Computational Modelling of Concrete Fracture, Doctoral Thesis, Technical University of Delft, p.132, 1988.
21. ACI 318-08, Building Code Requirements for Structural Concrete and Commentary, American Concrete Institute, Farmington Hills
22. Corley W.G. and Hawkins N.M, Shearhead Reinforcement for Slabs, ACI Structural Journal, Vol. 65, No. 10, 811-824, 1968.
23. Chana P.S and Birjandi F.K. Design guidance on structural steel shearheads in concrete, Project report for Reinforced Concrete Council and Department of the Environment, CRIC CLIENT REPORT CRIC95/001/F, Imperial College London, 1996.
24. BRITISH STANDARDS INSTITUTION. *European Standard EN-1992-1-1:2004, Eurocode 2: Design of Concrete Structures. Part 1, General Rules and Rules for Buildings*. BSI, 2004, London.
25. BRITISH STANDARDS INSTITUTION. *BS8110, Part 1:1997, Structural use of concrete: Code of practice for design and construction*. BSI, 2007, London

List of Tables

Table 1: Material properties used in baseline analysis for slab S1

Model	fc' [MPa]	ft [MPa]	fy [MPa]	εcu	Ec [MPa]	Gf [Nmm/mm^2]	Gc [Nmm/mm^2]	β	softening
Param1 (Base)	24	1.5	550	0.003	13500	0.058	11.60	0.25	exponential

Note: f_c'=concrete cylinder strength, f_t=concrete tensile strength, E_c = concrete elastic modulus, G_f = tensile fracture energy, G_c = compressive fracture energy and β=shear retention factor.

Table 2: Material properties used in analysis of slab H1

Model	fc' [MPa]	ft [MPa]	fy [MPa]	εcu	Ec [MPa]	Gf [Nmm/mm^2]	Gc [Nmm/mm^2]	β	softening
H1 Base	38	1.5	600	0.003	21075	0.067	6.7	0.1	exponential
H1† Sensiti-vity	38	1.89	600	0.003	21075	0.067	13.4	0.25	exponential
BN1	14.5	1.18	423	0.0025	9634	0.034	3.4	0.2	exponential
BH2	14.5	1.18	423	0.0025	9634	0.034	3.4	0.2	exponential
BH3	14.5	1.18	423	0.0025	9634	0.034	3.4	0.2	exponential

Note: † The material properties used in the sensitivity analysis have the same relationship with the concrete cylinder strength as those shown in Table 1.

Table 3: Measured and predicted response of specimens tested by Corley and Hawkins [22].

	L_v	V-test	V-predicted	V-pred/V-test	M† test	M† predicted NLFEA	Shearhead yield in test
	[mm]	[kN]	[kN]	[1]	[kNm]	[kNm]	-
BN-1*	-	265.56	258.00	0.97	-	-	-
BH-2	229	301.14	312.80	1.04	3.36	5.13	No
BH-3	457	402.14	405.00	1.01	9.48	9.71	Yes

Note: † Moment in shearhead at face of column.

List of Figures

Figure 17: Variation in predicted strains ε_{xx} at P_u=432kN over the depth of the slab at the intersection with the gusset plate.

Figure 18: Mode-1 crack contour levels in reinforcement layer at P_u=432kN

Figure 19a: Distribution of ε_{xx} over the depth of Slab S1 at the face of column for baseline model at ultimate load.

Figure 19b: Distribution of ε_{xx} over the depth of Slab S1 at the face of column for baseline model with shear head at ultimate load.

Figure 20a: Shear force distribution along shear arm in Slab H1 at P_u = 432 kN

Figure 20b: Calculated shearforce distribution along shear arm in Slabs BH2 and BH3 of Corley and Hawkins [22] at predicted failure load.

Figure 21: Bending moment distribution along shear arm in Slab H1 at P_u = 432 kN

Fig. 22a: ACI 318 [21] critical shear perimeter for large shear head and shear force distribution

Figure 22b: ACI 318 [21] shear force distribution along shearhead arms

Figure 22c: Chana and Birjandi [23] critical shear perimeter for enclosed shearhead

Figure 22d: Chana and Birjandi [23] critical shear perimeter for ACI 318 [21] shearhead

Figure 23: Comparison between measured and predicted shear strengths for tests of Corley and Hawkins [22]

Figure 24: Comparison between measured and predicted contribution of shear head for tests of Corley and Hawkins [22].

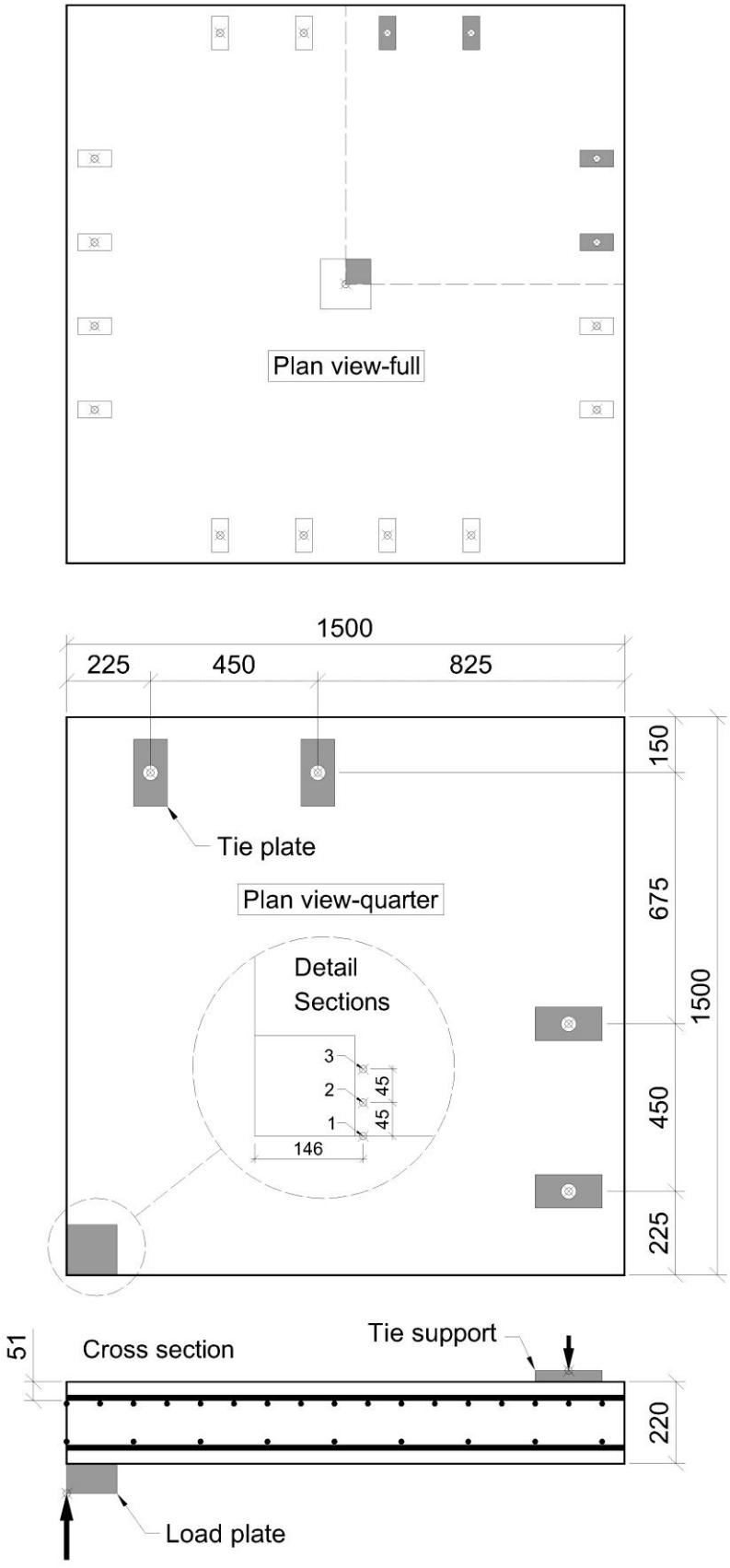

Figure 1: Geometry of finite element model used in baseline analysis for Slab S1

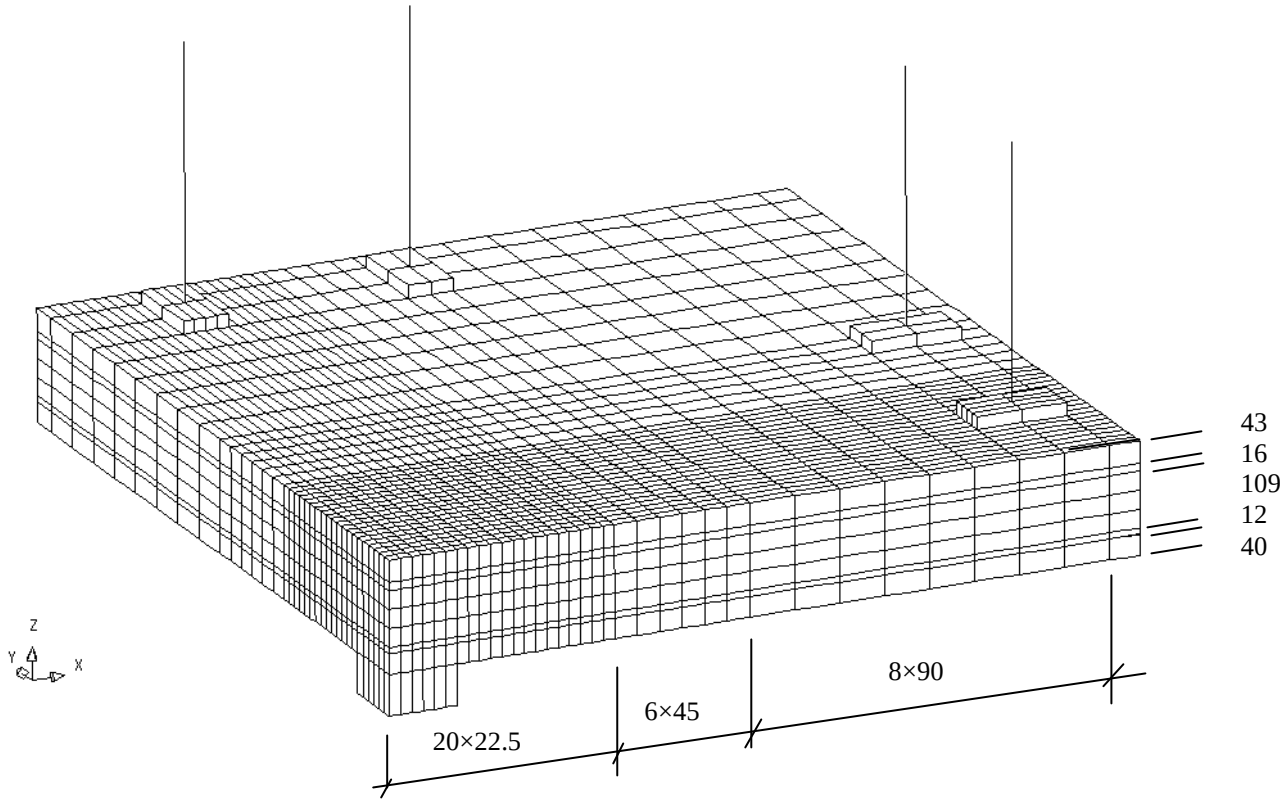

Figure 2: 3-D finite element mesh used in baseline model for Slab S1

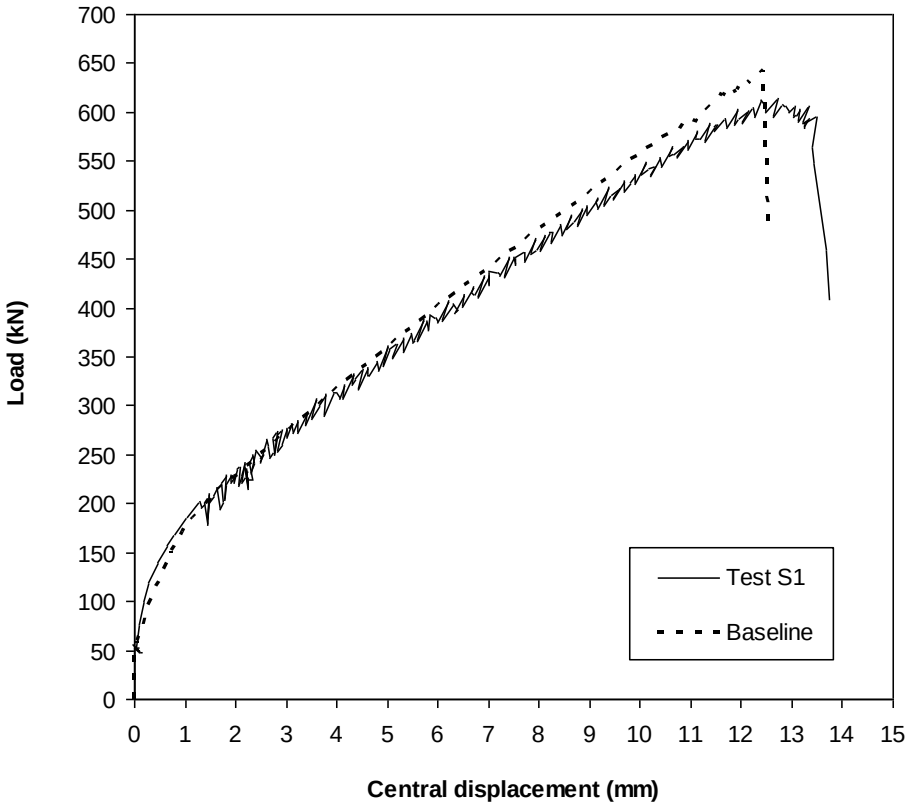

Figure 3: Comparison between measured and predicted (baseline) load-displacement response for Slab S1.

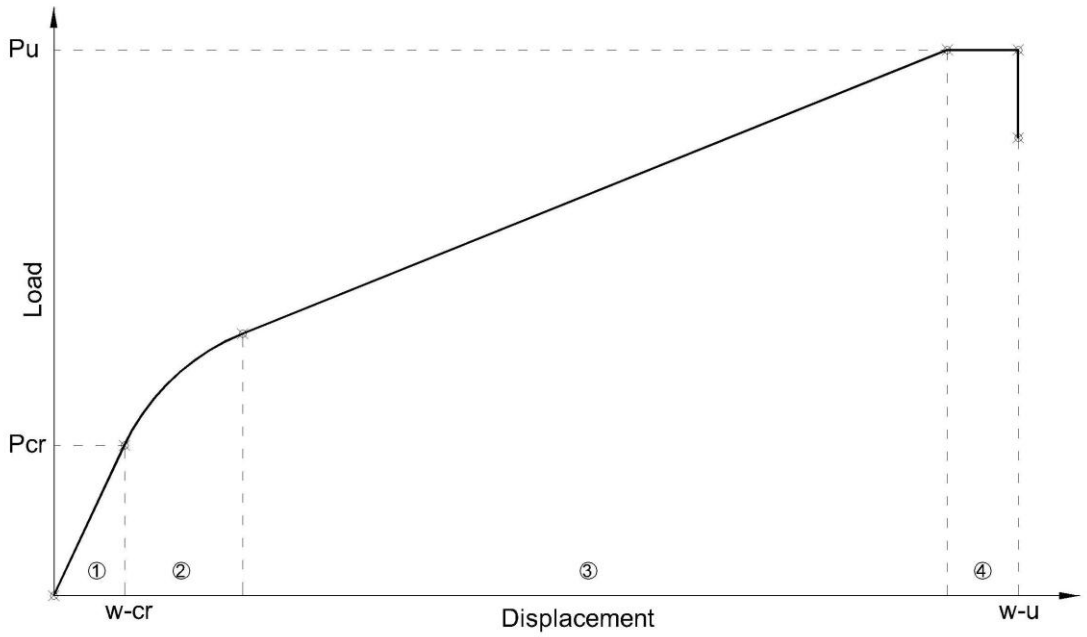

Figure 4: Idealised load displacement response for punching shear test

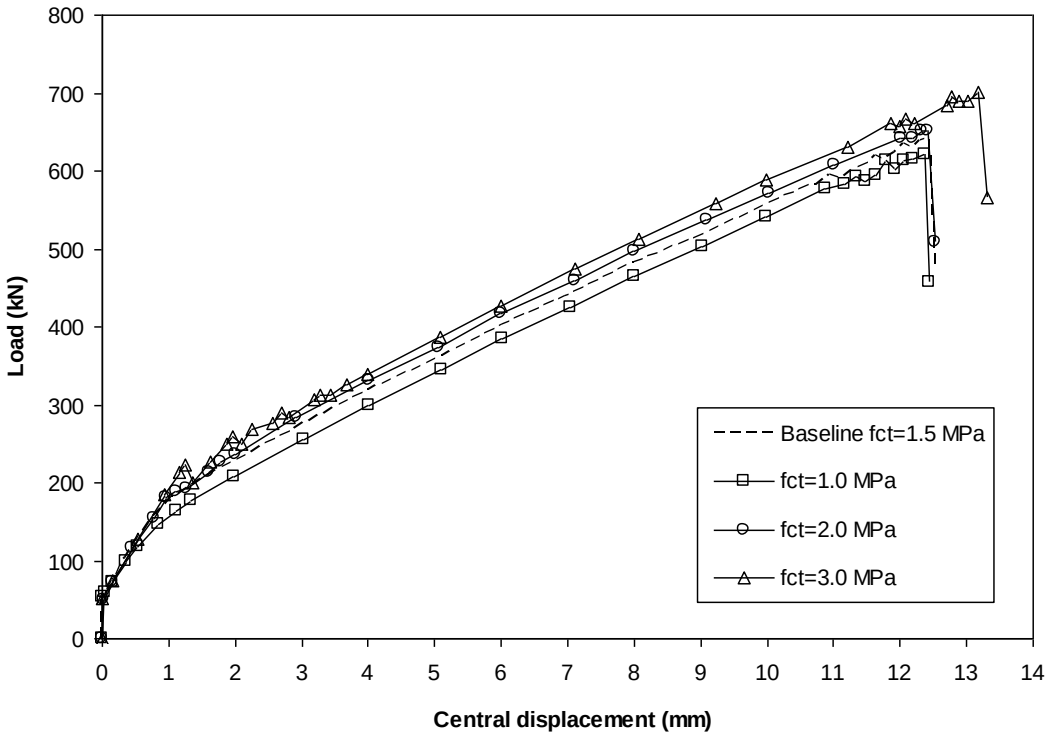

Figure 5: Influence of concrete tensile strength on predicted response of Slab S1

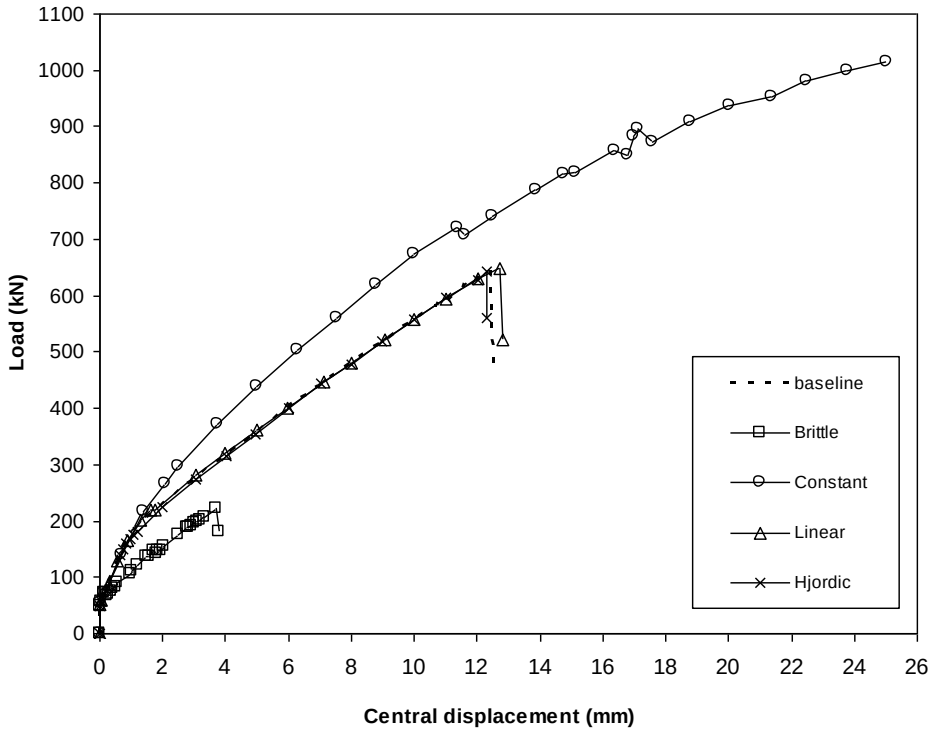

Figure 6: Influence of tension softening model on predicted response of Slab S1

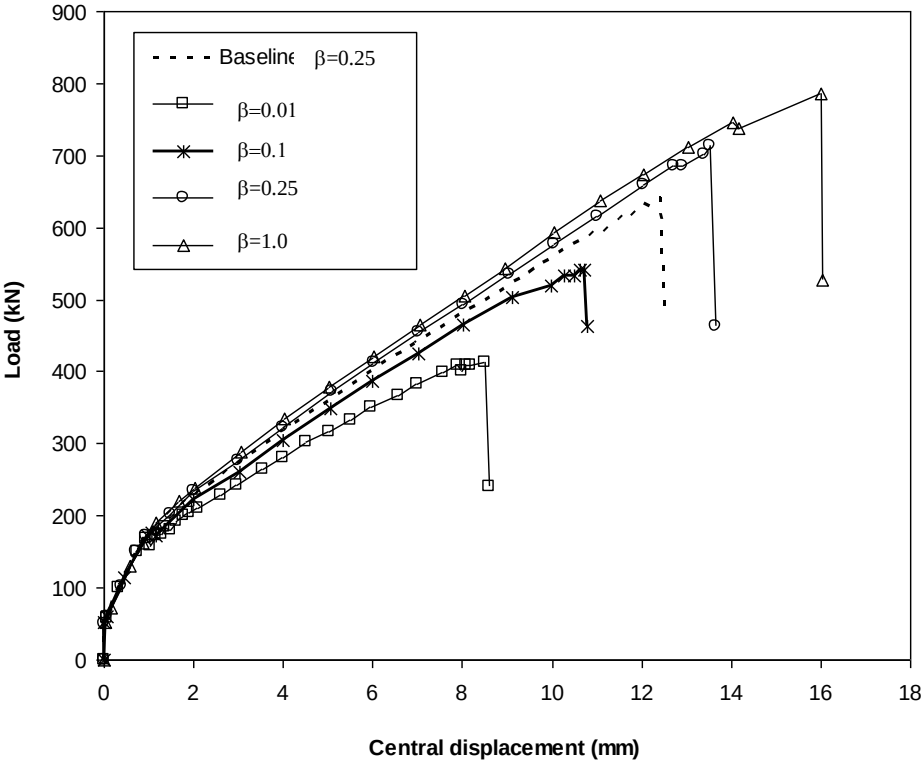

Figure 7: Influence of shear retention factor β on predicted response of Slab S1

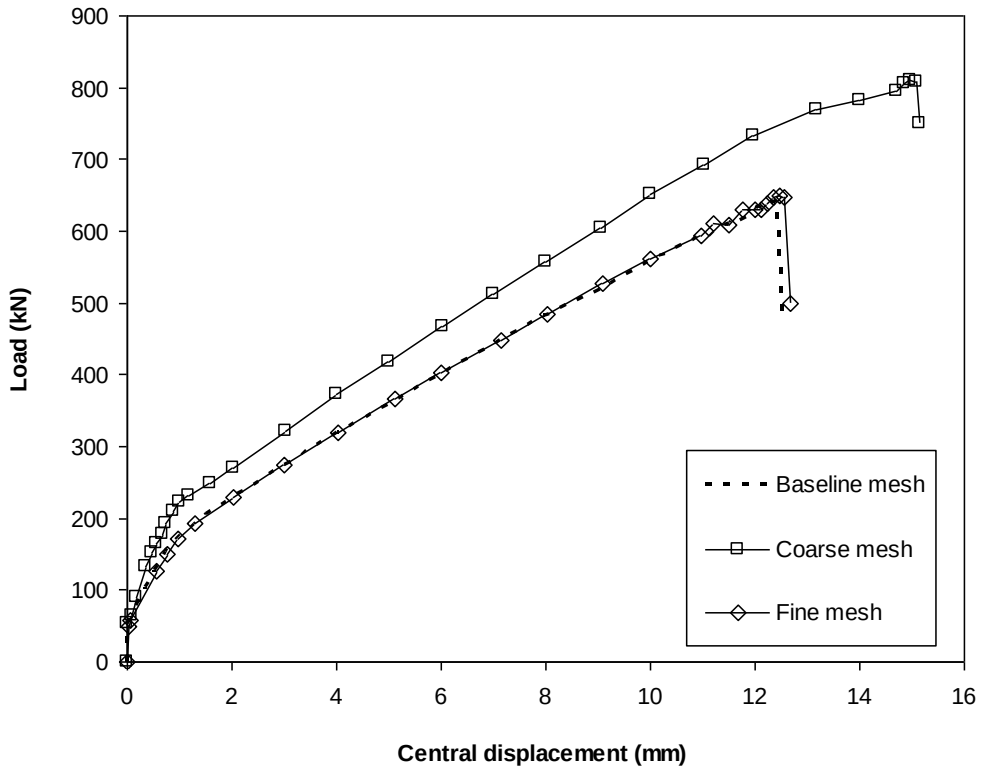

Figure 8: Influence of mesh size on predicted response of Slab S1

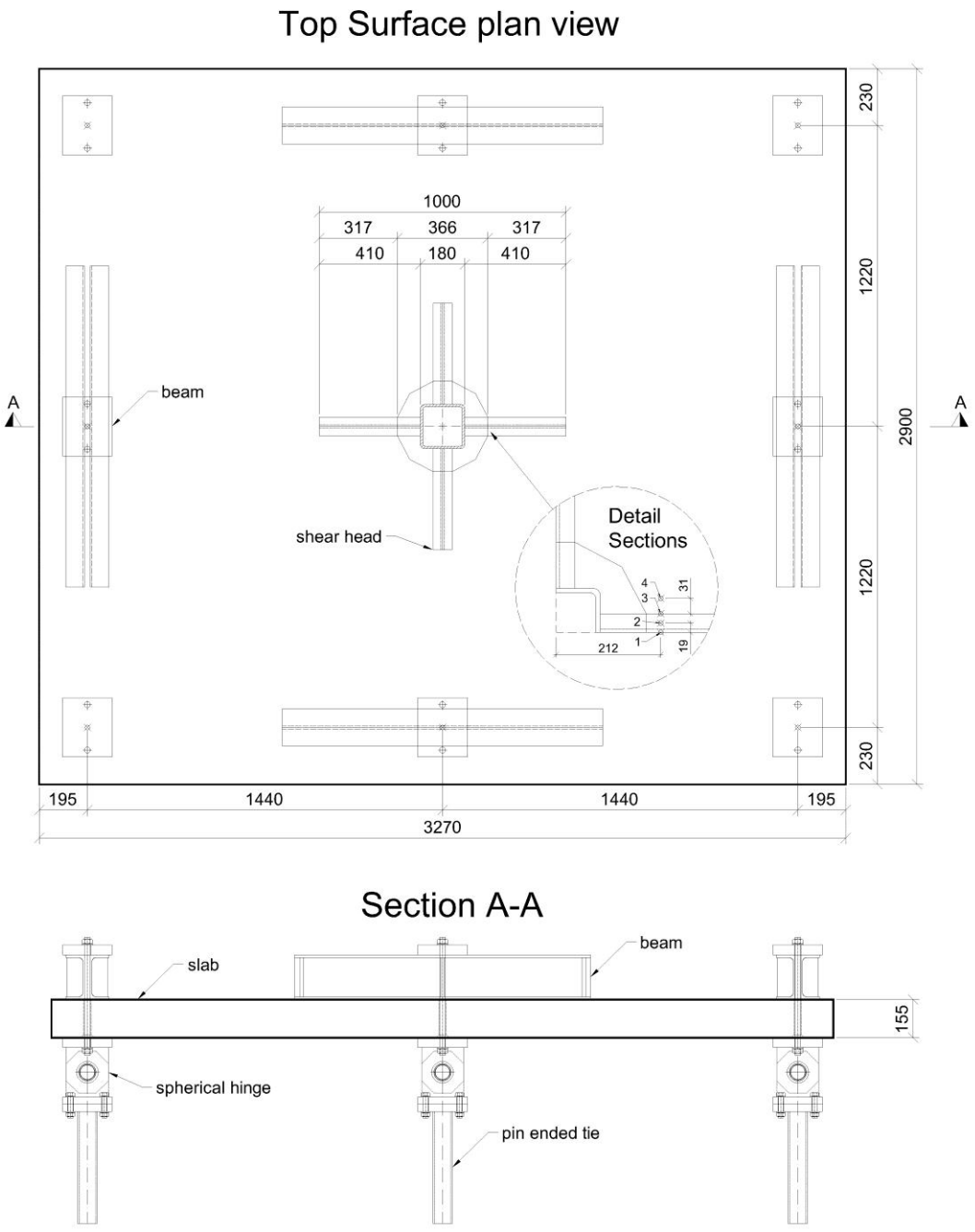

Figure 9a: Plan view of Specimen H1

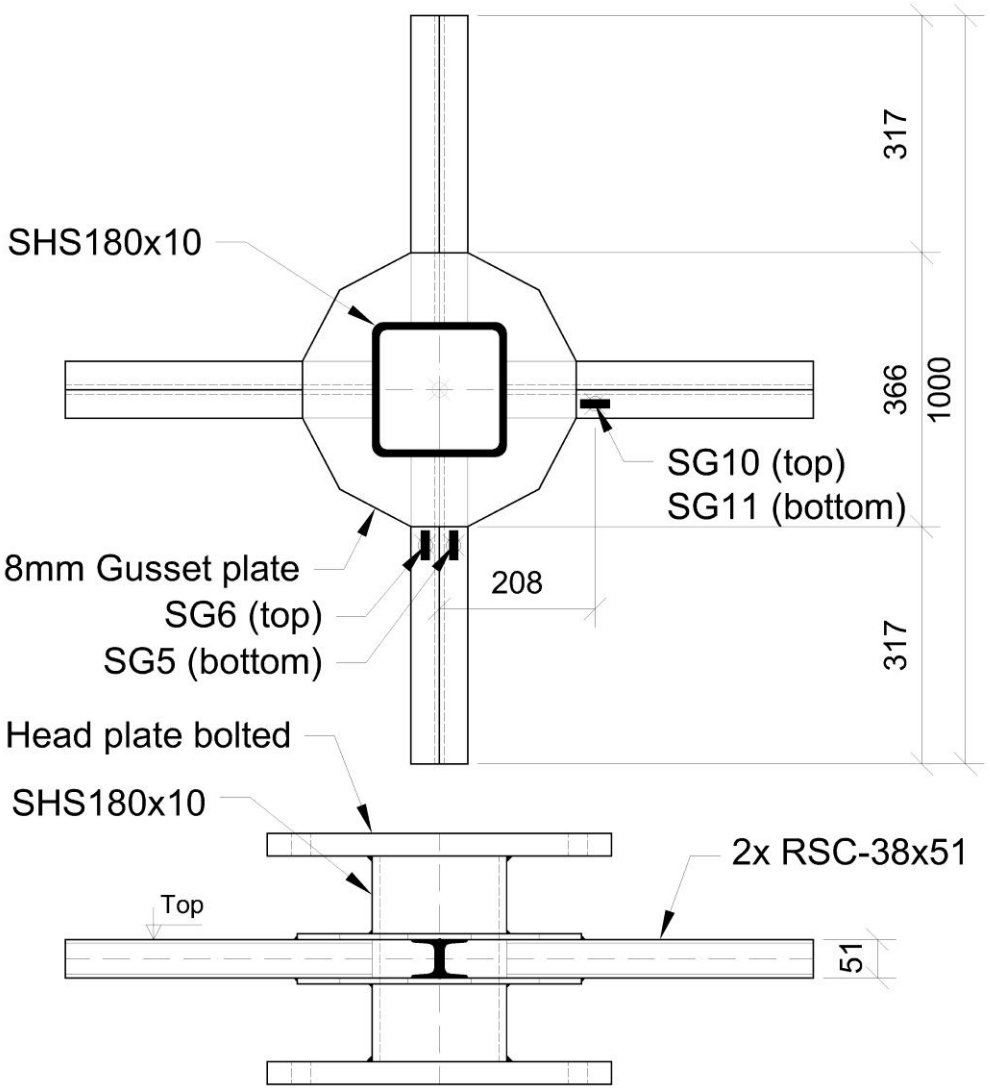

Figure 9b: Detail of shearhead

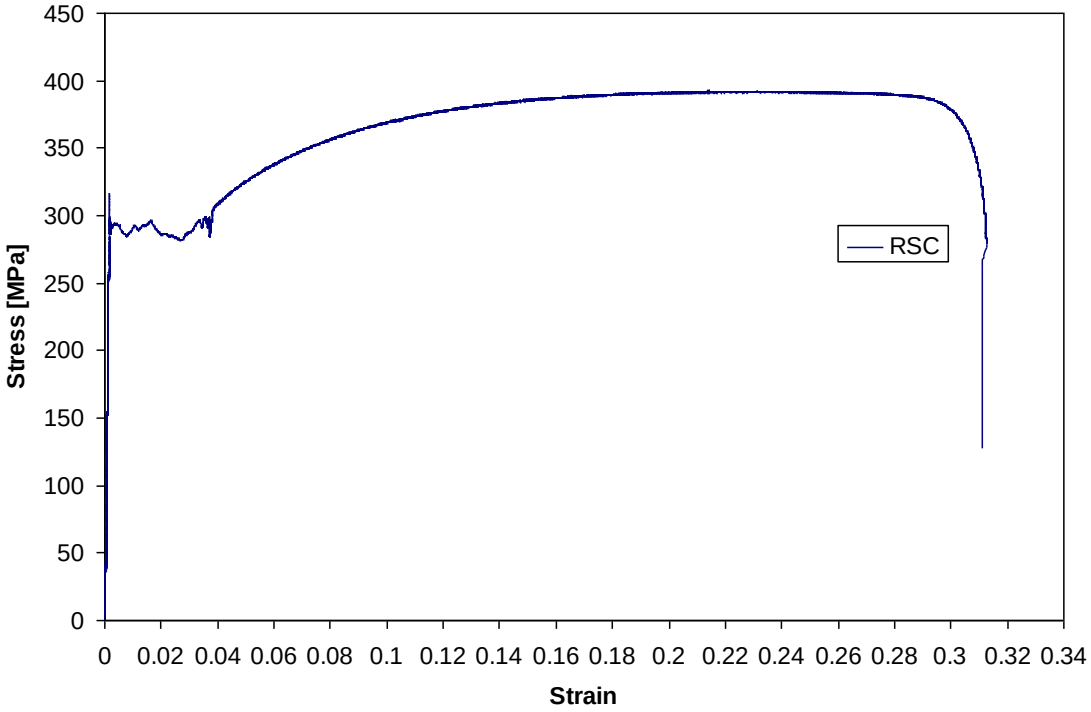

Figure 9c: Stress-strain diagram for shearhead

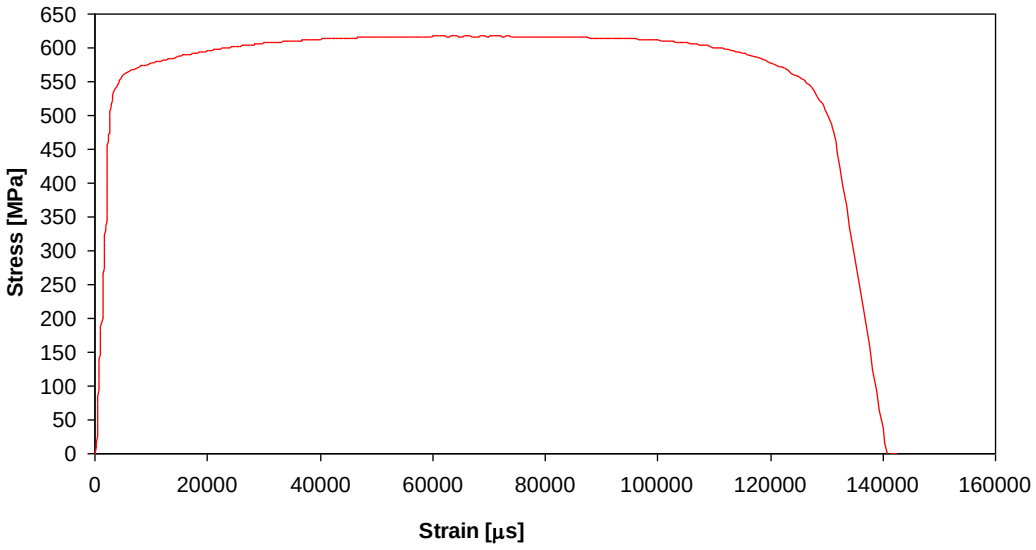

Figure 9d: Stress-strain diagram for H12 reinforcement bar

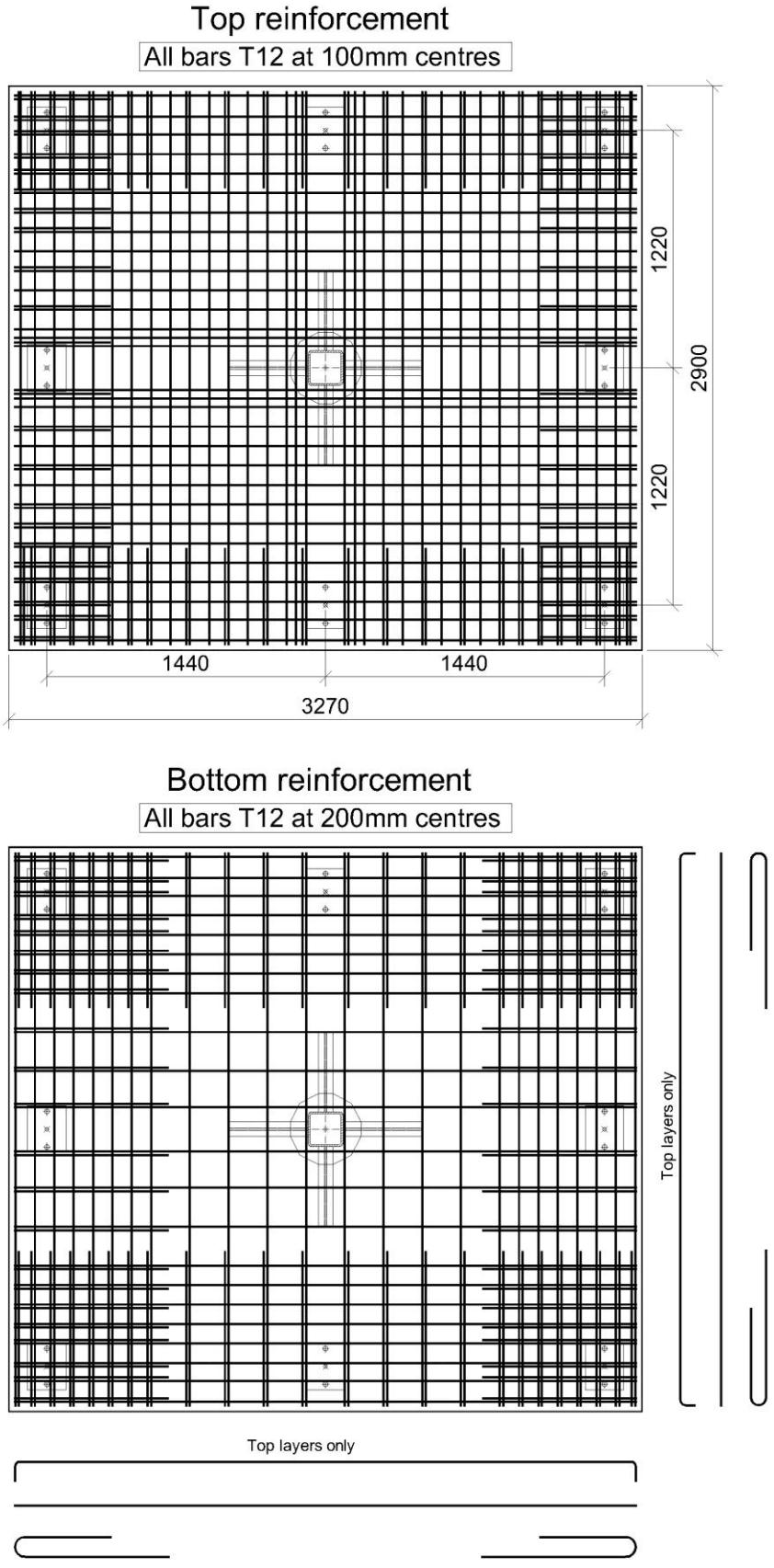

Figure 10: Reinforcement details for Slab H1 (cover 20mm to top and bottom reinforcement)

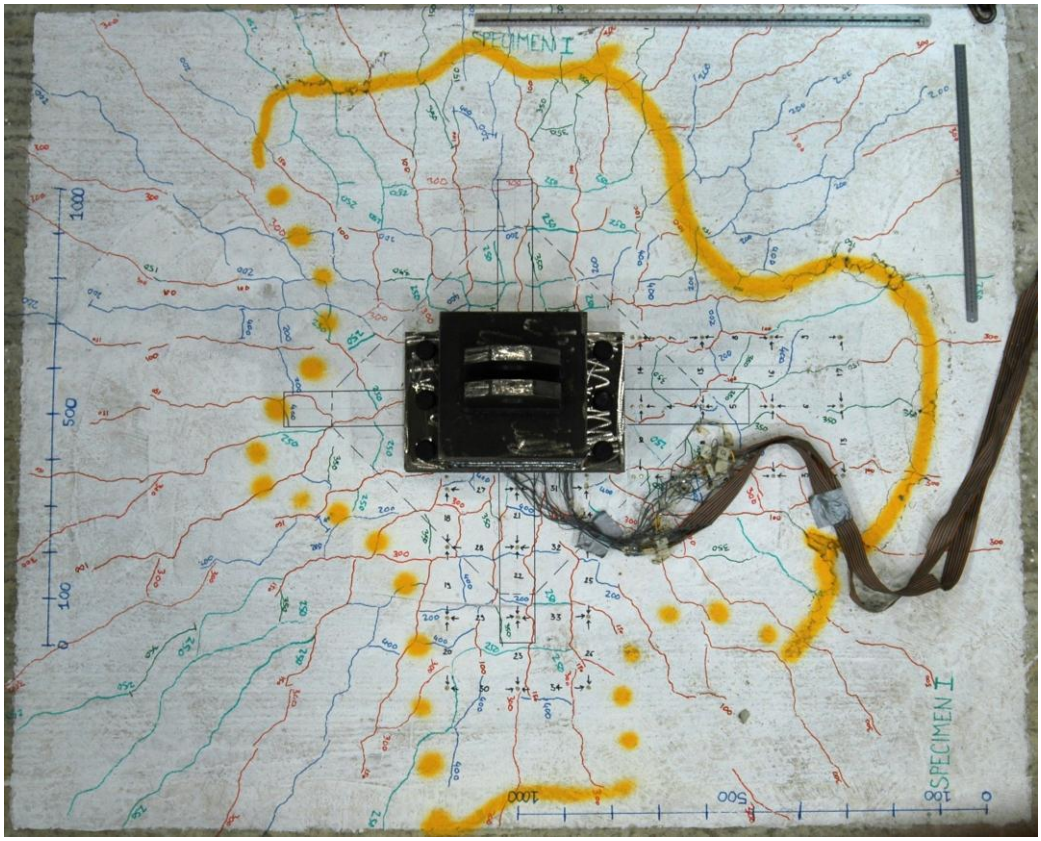

Figure 11: Crack pattern at failure for Slab H1

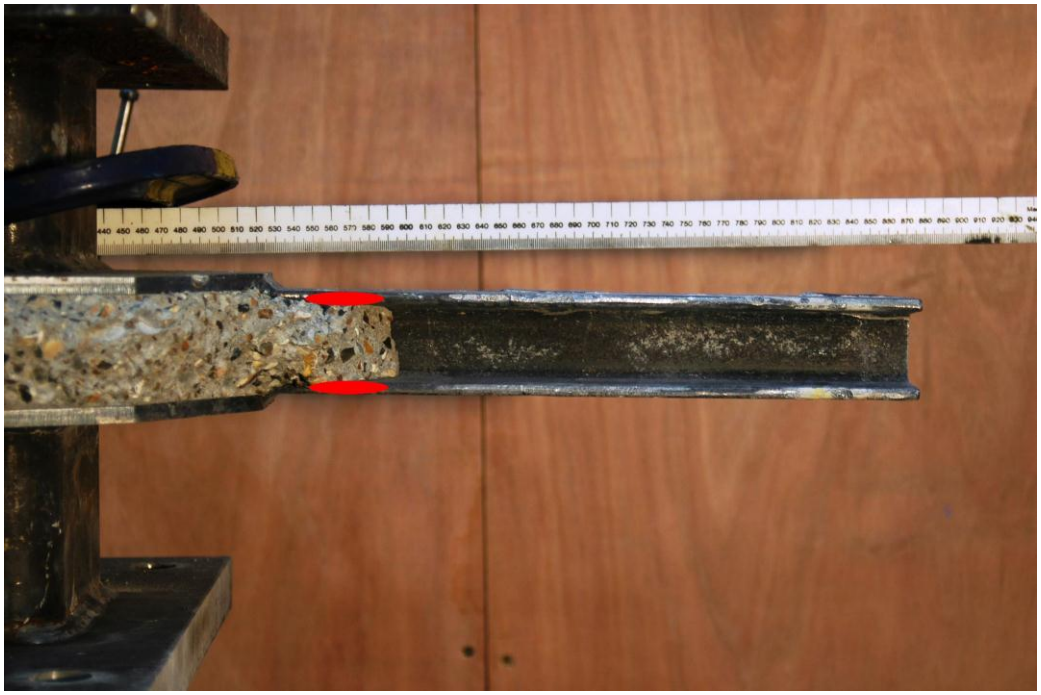

Figure 12: Deformed shape of shear head after test

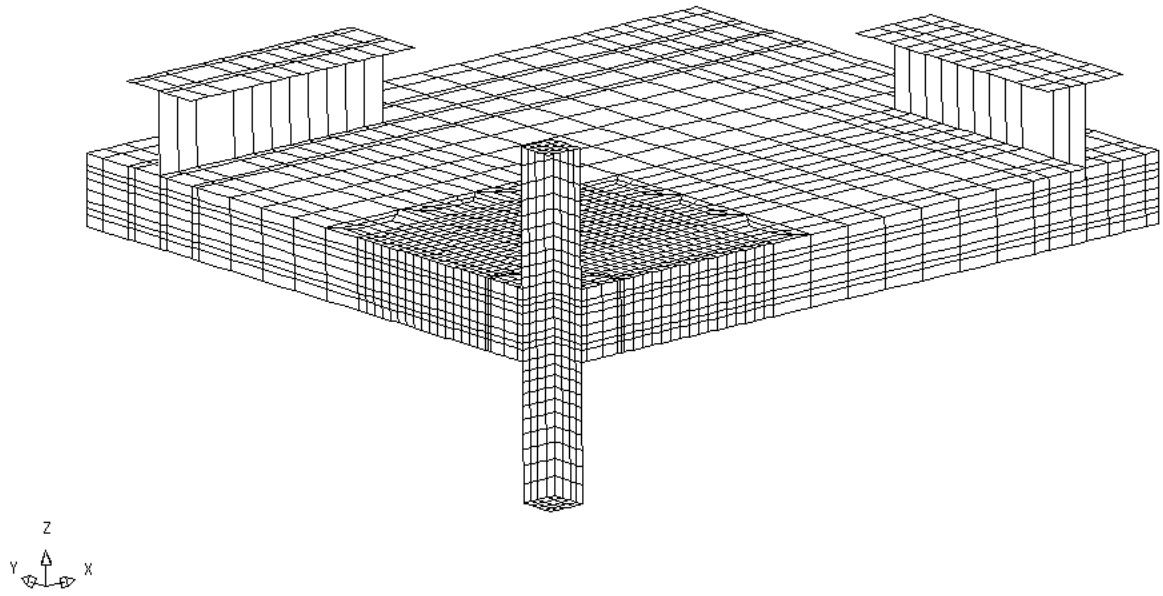

Figure 13a: Finite element mesh used to model Slab H1

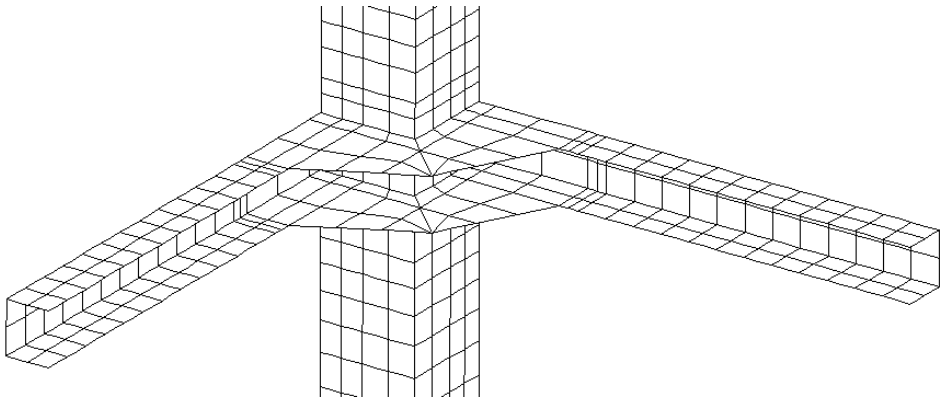

Figure 13b: Finite element mesh used to model shear head

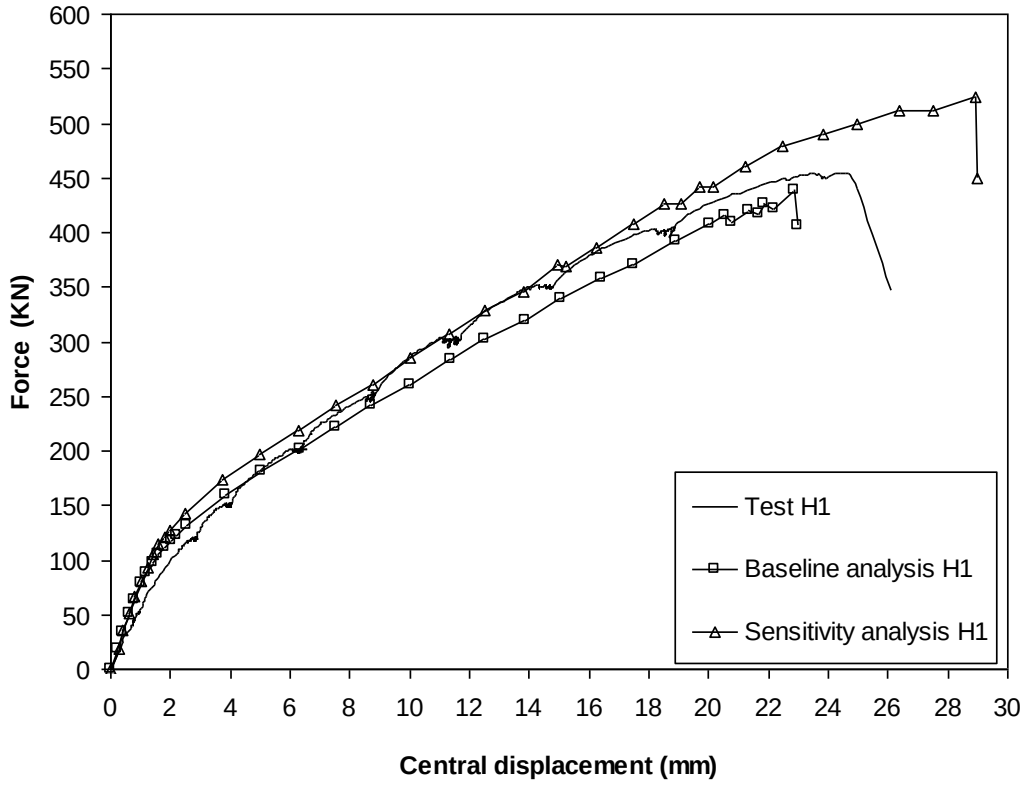

Figure 14: Comparison of measured and predicted load displacement response for Slab H1

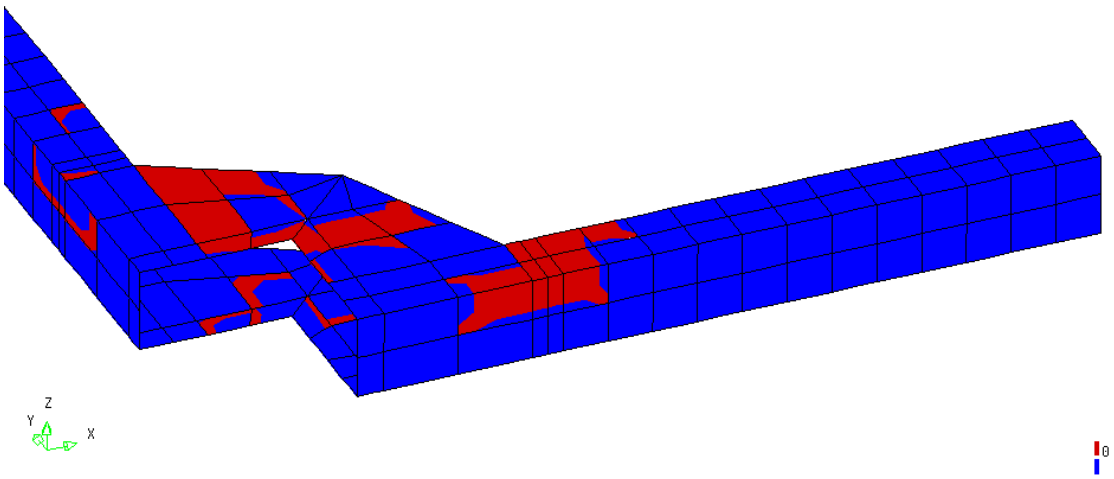

Figure 15: Computed plastic ε_{xx} strain distribution in the shear arm at P_u=432kN

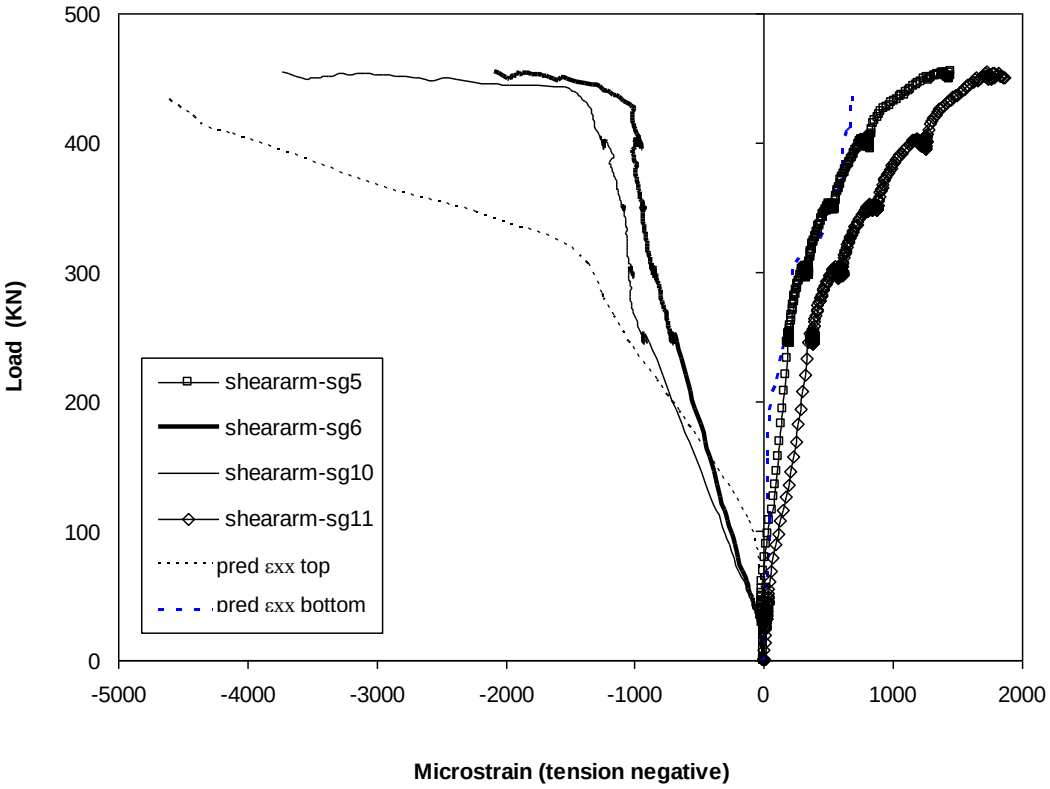

Figure 16: Comparison of measured and predicted strains in the top and bottom flanges of the shear head at the intersection with the gusset plate

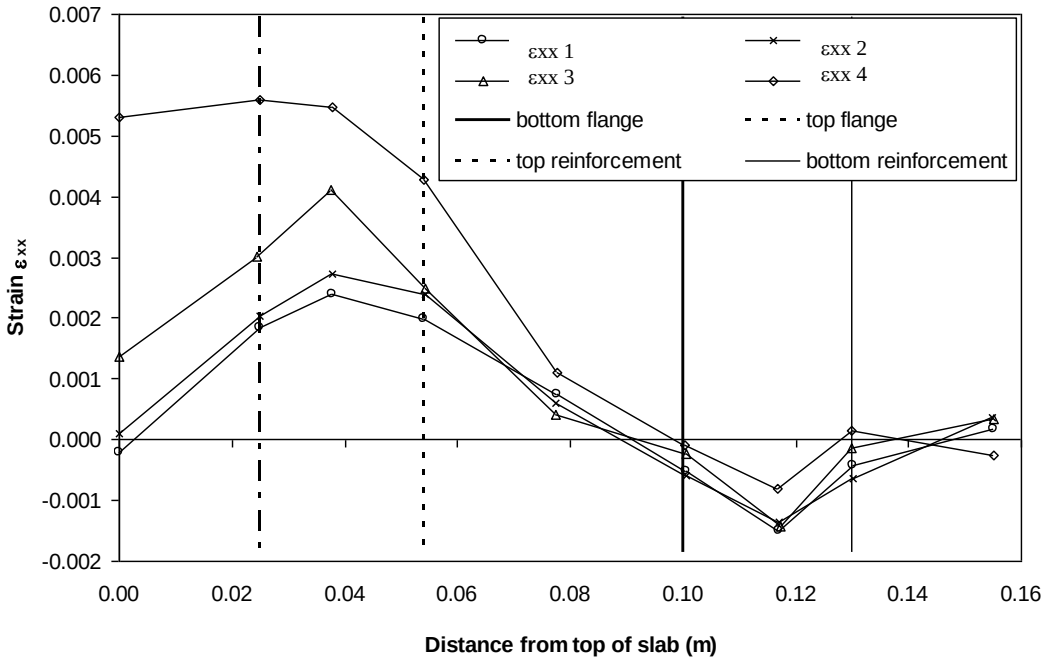

Figure 17: Variation in predicted strains ε_{xx} at P_u=432kN over the depth of the slab at the intersection with the gusset plate.

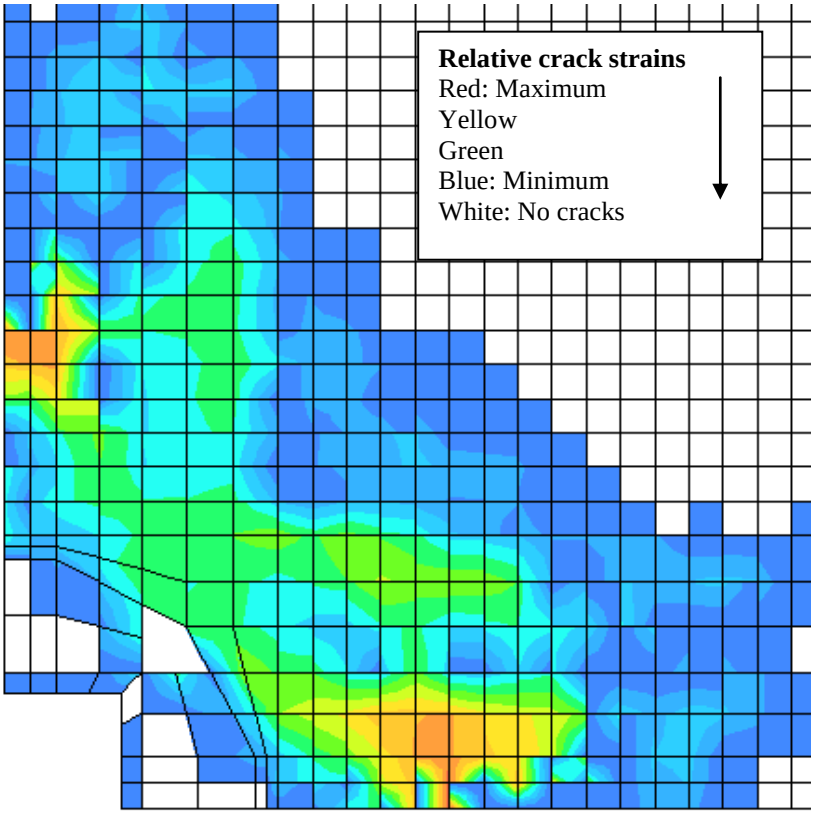

Figure 18: Mode-1 (almost horizontal) crack contour levels in reinforcement layer at at P_u=432kN

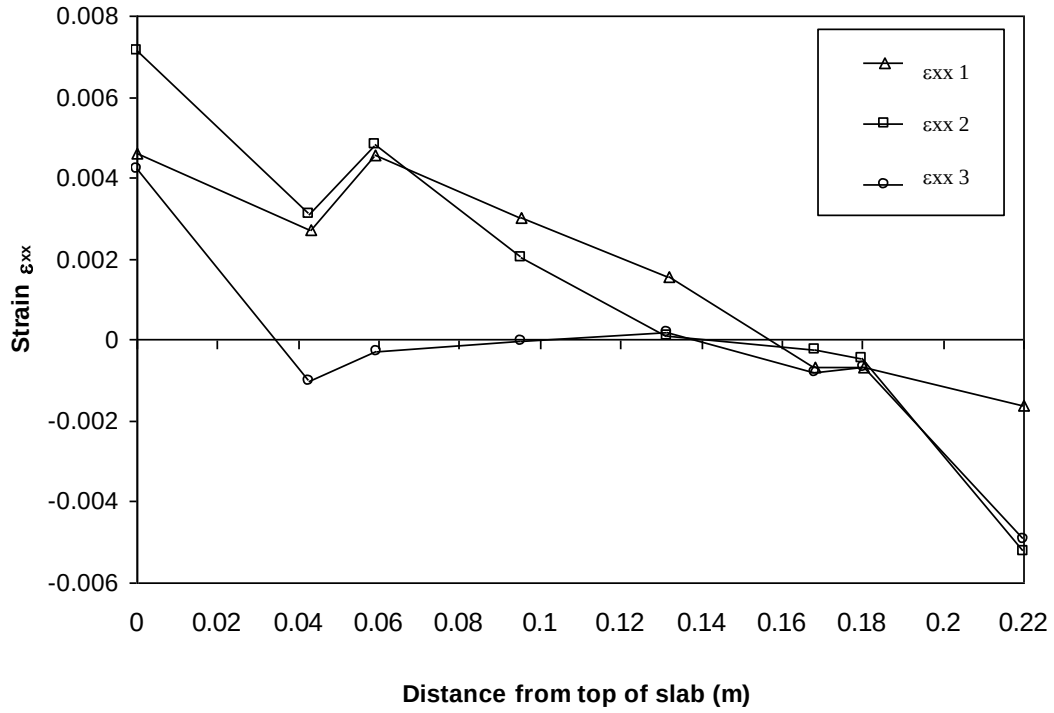

Figure 19a: Distribution of ε_{xx} over the depth of Slab S1 at the face of column for baseline model at ultimate load.

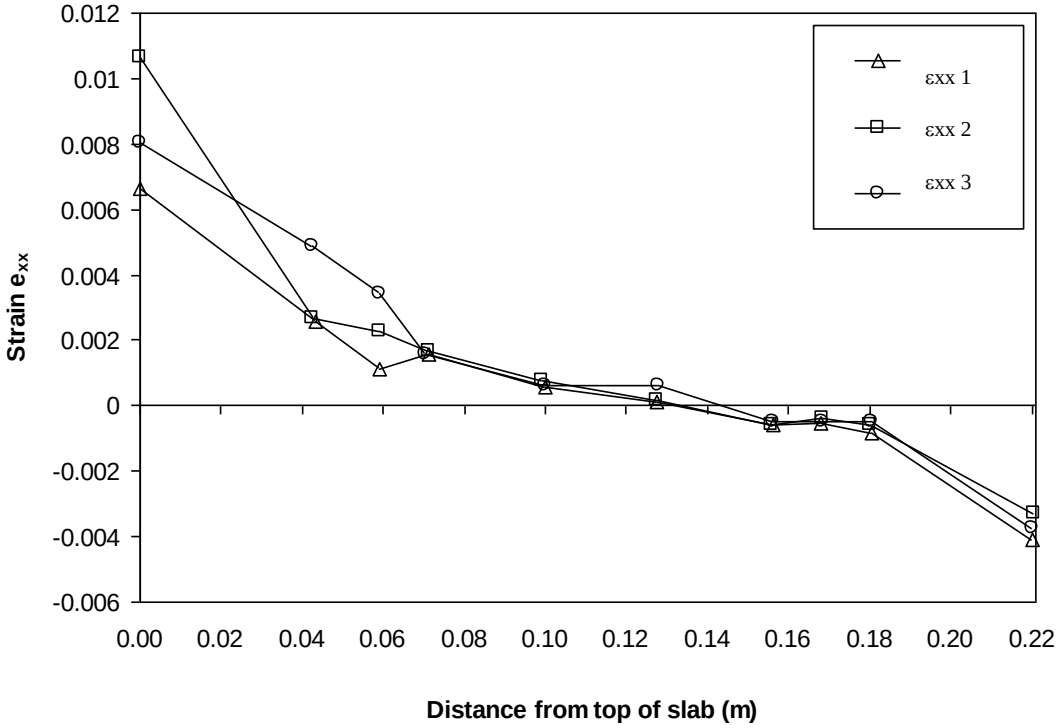

Figure 19b: Distribution of ε_{xx} over the depth of Slab S1 at the face of column for baseline model with shear head at ultimate load.

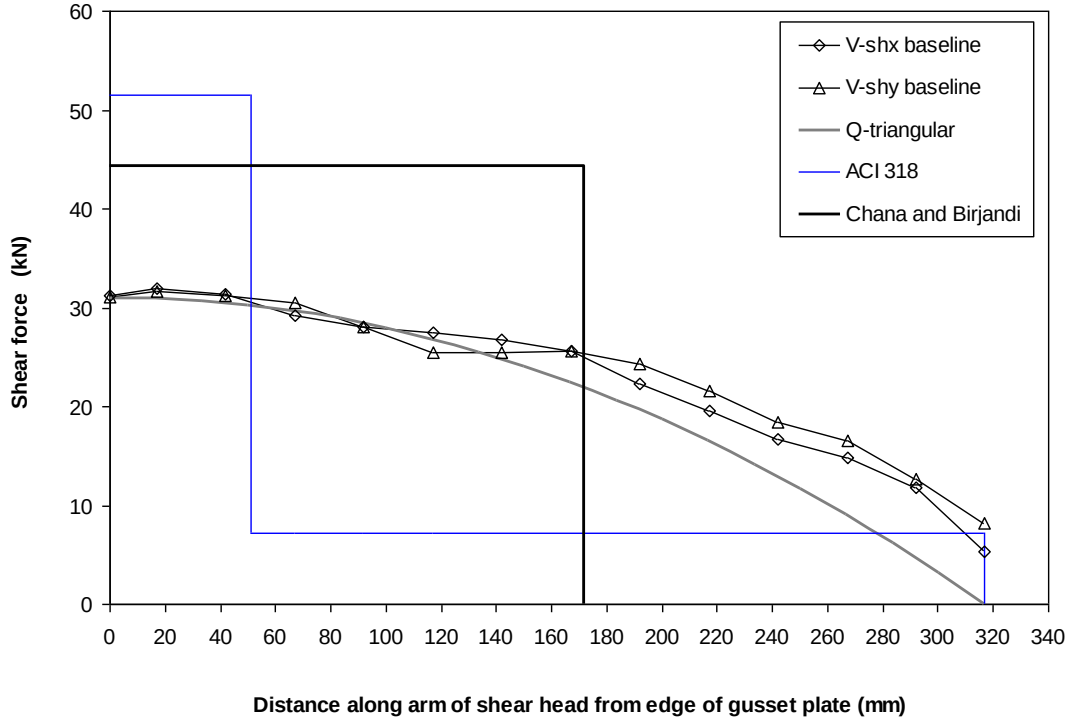

Figure 20a: Shear force distribution along shear arm in Slab H1 at P_u = 432 kN

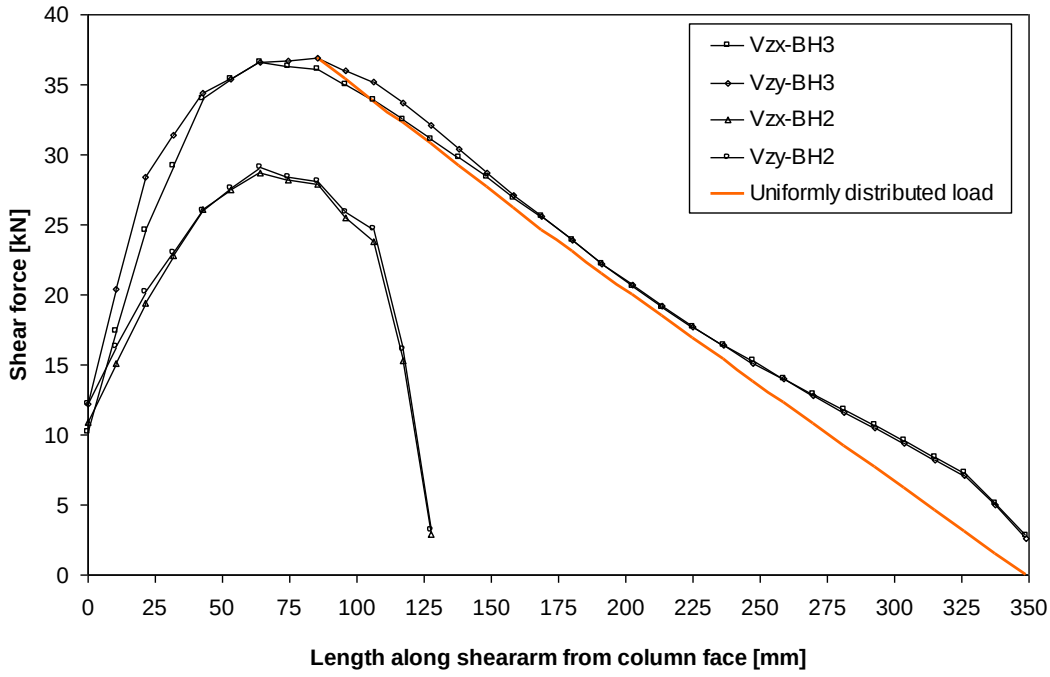

Figure 20b: Calculated shearforce distribution along shear arm in Slabs BH2 and BH3 of Corley and Hawkins [22] at predicted failure load.

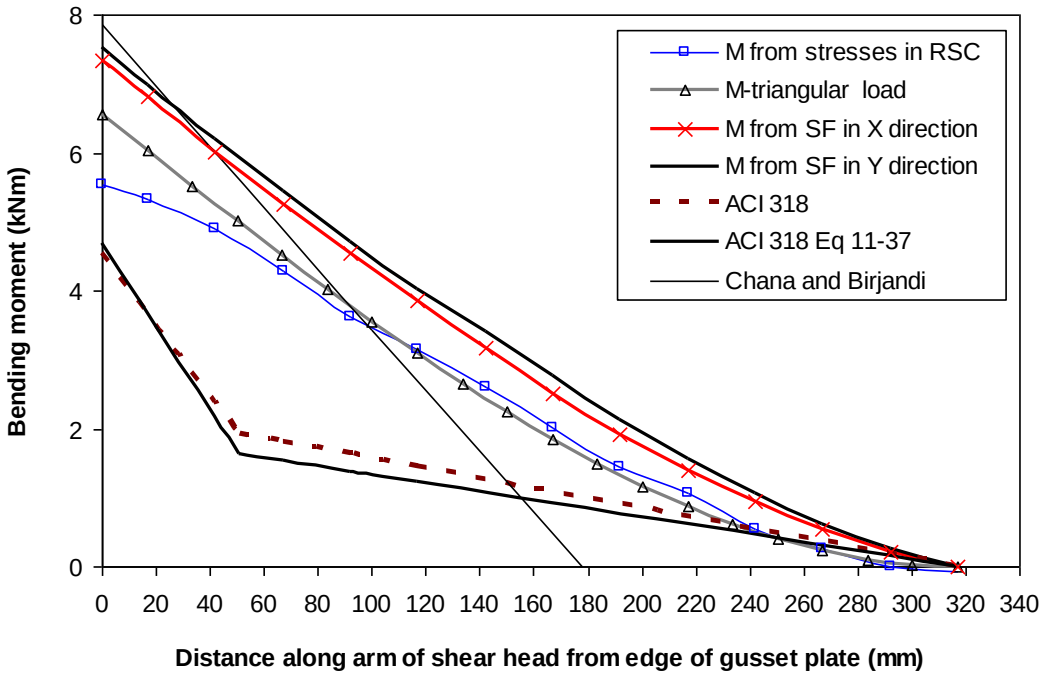

Figure 21: Bending moment distribution along shear arm in Slab H1 at P_u = 432 kN

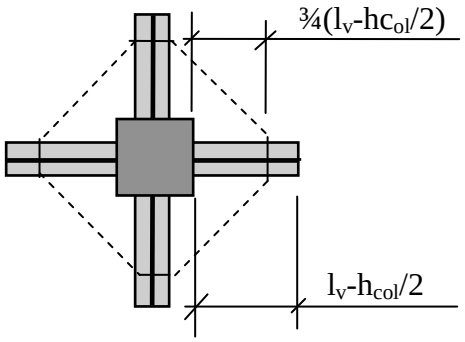

Fig. 22a: ACI 318 [21] critical shear perimeter for large shear head and shear force distribution

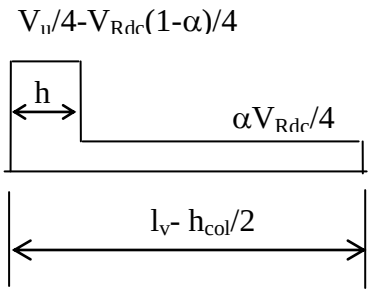

Note: h = depth of shearhead arms

Figure 22b: ACI 318 [21] shear force distribution along shearhead arms

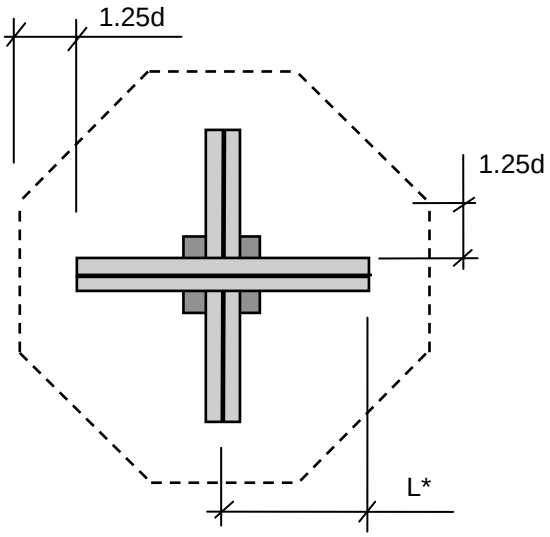

Figure 22c: Chana and Birjandi [23] critical shear perimeter for enclosed shearhead

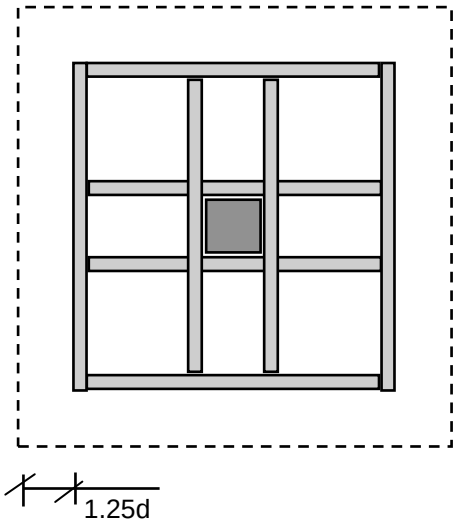

Figure 22d: Chana and Birjandi [23] critical shear perimeter for ACI 318 [21] shearhead

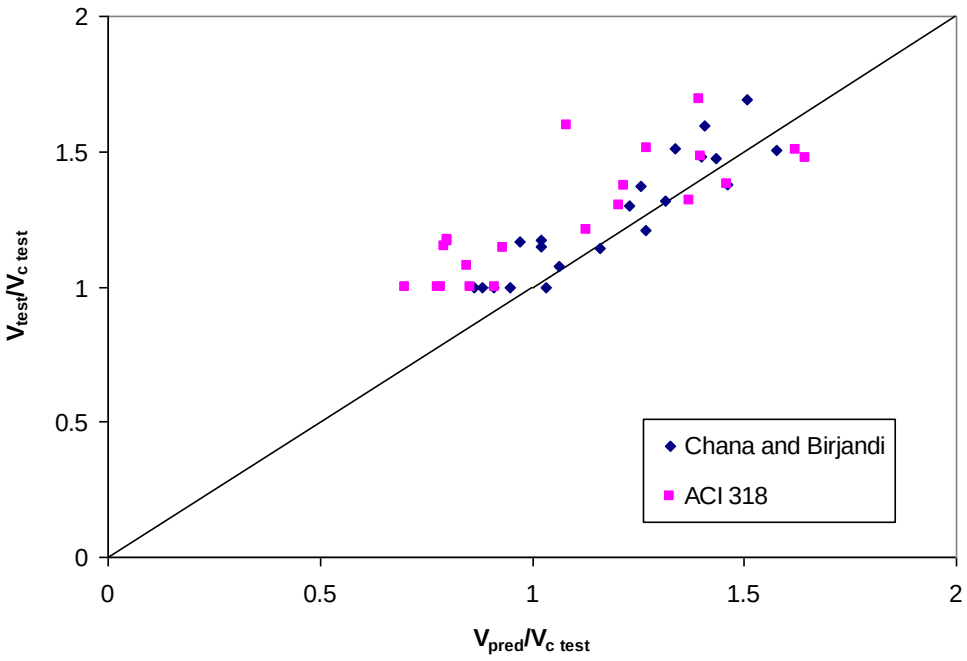

Figure 23: Comparison between measured and predicted shear strengths for tests of Corley and Hawkins [22].

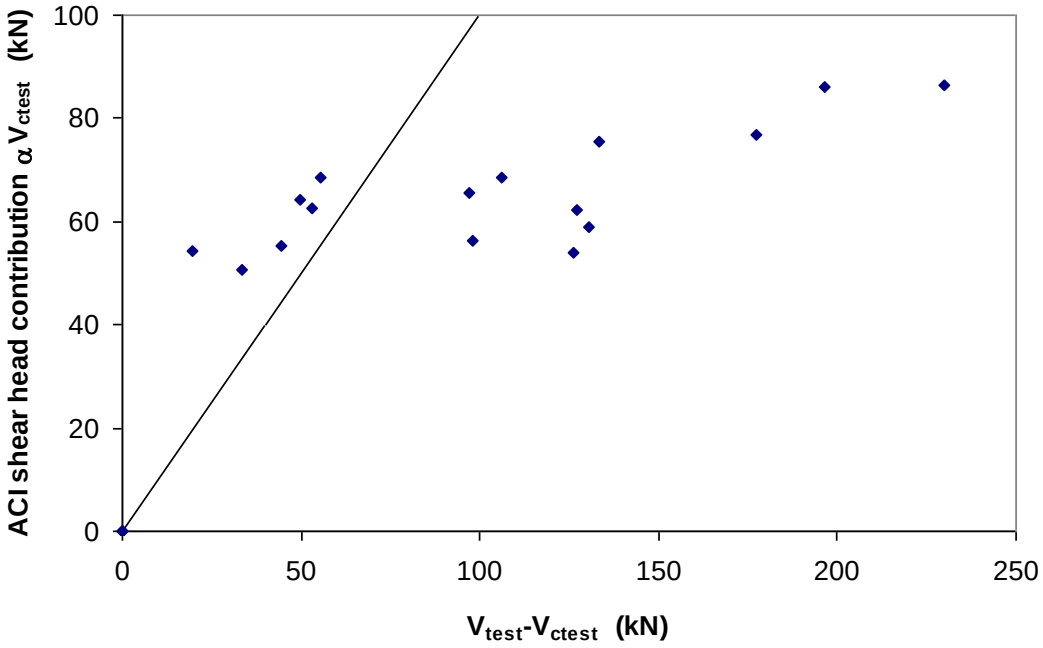

Figure 24: Comparison between measured and predicted contribution of shear head for tests of Corley and Hawkins [22].